*nanomaterials*

MDPI

*Review*

# Graphitic Carbon Nitride-Based Heterojunctions for Photocatalytic Water Purification: Mechanisms, Fabrication, and Applications

**Jinhua Zhuang [1], Heshan Cai [1,*], Sibo Ding [1], Zekai Liu [1], Haopeng Liao [1], Haoze Jiang [1], Yuyue Luo [1], Chaoming Liang [1], Hang Zhang [1], Songran Guan [1] and Daguang Li [2,*]**

[1] School of Environmental and Chemical Engineering, Foshan University, Foshan 528200, China
[2] College of Light Chemical Industry and Materials Engineering, Shunde Polytechnic University, Foshan 528300, China
* Correspondence: caiheshan@foxmail.com (H.C.); ldguang918@163.com (D.L.)

**Abstract**

As a metal-free, visible-light-responsive two-dimensional (2D) layered semiconductor, graphitic carbon nitride (g-$C_3N_4$) has been extensively studied for photocatalytic water purification owing to its high chemical stability, facile synthesis, and low cost. However, single-phase g-$C_3N_4$ still suffers from bottlenecks including rapid photogenerated electron–hole pair recombination, low visible-light utilization efficiency, insufficient specific surface area, and a limited number of exposed surface active sites, which severely restrict its practical photocatalytic performance. Rational construction of heterojunctions with matched band alignment and intimate interfacial contact serves as an effective strategy to boost the photocatalytic activity of g-$C_3N_4$. This review introduces the structural characteristics and photocatalytic mechanisms of g-$C_3N_4$, summarizes the primary types of g-$C_3N_4$-based heterojunctions along with their charge transfer pathways, and highlights recent research progress in emerging contaminant degradation, pathogenic microbial disinfection, and reduction of high-valence and highly toxic heavy-metal ions for water decontamination. The review closes with critical perspectives on the rational design and practical engineering prospects of g-$C_3N_4$-based heterojunctions. By bridging heterojunction mechanisms with water-purification applications and engineering considerations, this review is expected to guide the rational design of high-performance g-$C_3N_4$-based heterojunctions and accelerate their translation toward practical water purification.

**Keywords:** graphitic carbon nitride; heterojunction; photocatalysis; pollutants; water purification applications

Check for updates

Academic Editor: Marco Stoller

Received: 29 September 2026
Revised: 21 October 2026
Accepted: 23 October 2026
Published: 26 October 2026

**Copyright:** © 2026 by the authors. Licensee MDPI, Basel, Switzerland. This article is an open access article distributed under the terms and conditions of the Creative Commons Attribution (CC BY) license.

## 1. Introduction

In recent years, industrial and municipal discharges have rendered aquatic pollution increasingly complex, featuring emerging contaminants, pathogenic microorganisms, and heavy metal ions. Emerging contaminants, including antibiotics, endocrine-disrupting chemicals (EDCs), and microplastics, are continuously discharged into the environment, exhibit complex migration-transformation behaviors and pose uncertain ecological risks; highly toxic heavy metal species and microbial pathogens pose severe chemical toxicity and biosafety hazards, respectively [1]. Conventional water treatment technologies (e.g., adsorption, coagulation, and biological treatment) offer limited removal capability toward recalcitrant and highly toxic pollutants, frequently accompanied by incomplete

mineralization, secondary pollution risks, and poor adaptability toward complex matrices, failing to meet demands for deep-level water purification [2,3]. Consequently, developing efficient, green, and sustainable water purification technologies has become an urgent environmental priority [4].

Photocatalytic technology utilizes solar energy to drive redox reactions and represents an environmentally benign pathway for pollutant degradation, microbial disinfection, and high-valence metal ion reduction. As an archetypal metal-free polymeric semiconductor, g-$C_3N_4$ features a bandgap of ~2.7 eV, visible-light responsiveness, high chemical stability, earth-abundant raw materials, and facile synthesis, rendering it one of the most intensively studied materials for photocatalytic water purification [5]. Nevertheless, pristine g-$C_3N_4$ is restricted by inherent performance bottlenecks, and single-component systems struggle to fulfill practical water treatment requirements. Coupling g-$C_3N_4$ with band-matched semiconductors to engineer heterojunctions can effectively manipulate carrier migration pathways and improve charge separation efficiency, representing an effective strategy for enhancing its photocatalytic activity [6,7]. Since the landmark report by Wang et al. [8] establishing graphitic carbon nitride as a visible-light-active metal-free polymeric semiconductor, g-$C_3N_4$-based systems have garnered immense interest. Driven by these advantages, g-$C_3N_4$-based heterojunctions offer substantial research value and broad application potential in water decontamination [9].

This review systematically summarizes recent advances in g-$C_3N_4$-based heterojunctions for photocatalytic water purification. The literature selection followed the PRISMA 2020 guidelines (Figure 1). A total of 864 records published between 2015 and 2026 were identified from the Web of Science Core Collection (*n* = 412), Scopus (n = 328), and Google Scholar (n = 124). After removing 216 duplicates, 648 records were screened by title and abstract, of which 456 were excluded (184 non-photocatalytic studies, 152 studies not involving water matrices, and 120 studies not based on g-$C_3N_4$). The remaining 192 articles were assessed in full text, and 74 were excluded (31 secondary reviews, 28 studies with unverified kinetics, and 15 studies reporting incomplete experimental conditions), leaving 118 primary experimental studies for quantitative synthesis and mechanistic benchmarking. The search string applied in the Web of Science and Scopus was ((“graphitic carbon nitride” OR “g-$C_3N_4$” OR “$C_3N_4$”) AND (heterojunction OR “type-I” OR “type-II” OR “Z-scheme” OR “S-scheme”) AND (photocatal) AND (water OR wastewater OR pollutant OR degradation OR disinfection OR antibacterial))). Google Scholar was searched with the simplified string “graphitic carbon nitride” AND heterojunction AND photocatalysis AND (water OR wastewater). The search was limited to English-language journal articles; reviews, conference abstracts, editorials, and studies without original experimental photocatalytic data were excluded. The discussion begins with the intrinsic structural characteristics and basic photocatalytic mechanisms of g-$C_3N_4$, followed by an in-depth analysis of the electronic transfer pathways of distinct heterojunction configurations and a systematic categorization of mainstream fabrication protocols, including chemical vapor deposition, hydrothermal/solvothermal methods, thermal calcination, In Situ Polymerization and Deposition–Precipitation and Electrostatic/Ultrasonication Assembly and Photodeposition. Practical implementations in degrading emerging pollutants, inactivating pathogens and reducing toxic heavy metals are then reviewed, and constructive perspectives and future recommendations are provided in closing to serve as valuable references for subsequent investigations in this field [10]. The g-$C_3N_4$-based photocatalysis has been surveyed from multiple angles in recent years, covering homojunctions [11], carbon nitride/graphene composites for emerging pollutant degradation [12], mechanistic comparisons of type-II, Z-scheme and S-scheme heterojunctions [13], Z-scheme catalysts for microplastics mineralization [14], morphology-controlled g-$C_3N_4$/metal oxide nanostructures [15], pharmaceutical

and antibiotic degradation [16–18], g-$C_3N_4$/Bi-based Z-scheme systems for the removal of pharmaceuticals and personal care products [19], and S-scheme heterojunctions for U(VI) reduction [20]. Distinct from existing reviews that survey single applications or material families, the novelty of this review is anchored in establishing an integrative 'mechanism-fabrication-engineering' framework. Specifically, this review uniquely provides: (i) an uncompromising critical assessment of the experimental validity of claimed Type-I, Type-II, Z-scheme, and S-scheme charge-transfer pathways; (ii) a multi-dimensional benchmarking matrix across fabrication routes balancing interface quality with industrial scalability; and (iii) a pragmatic water-treatment assessment that integrates practical water-matrix interferences, reaction byproducts, and reactor modeling into catalytic evaluations.

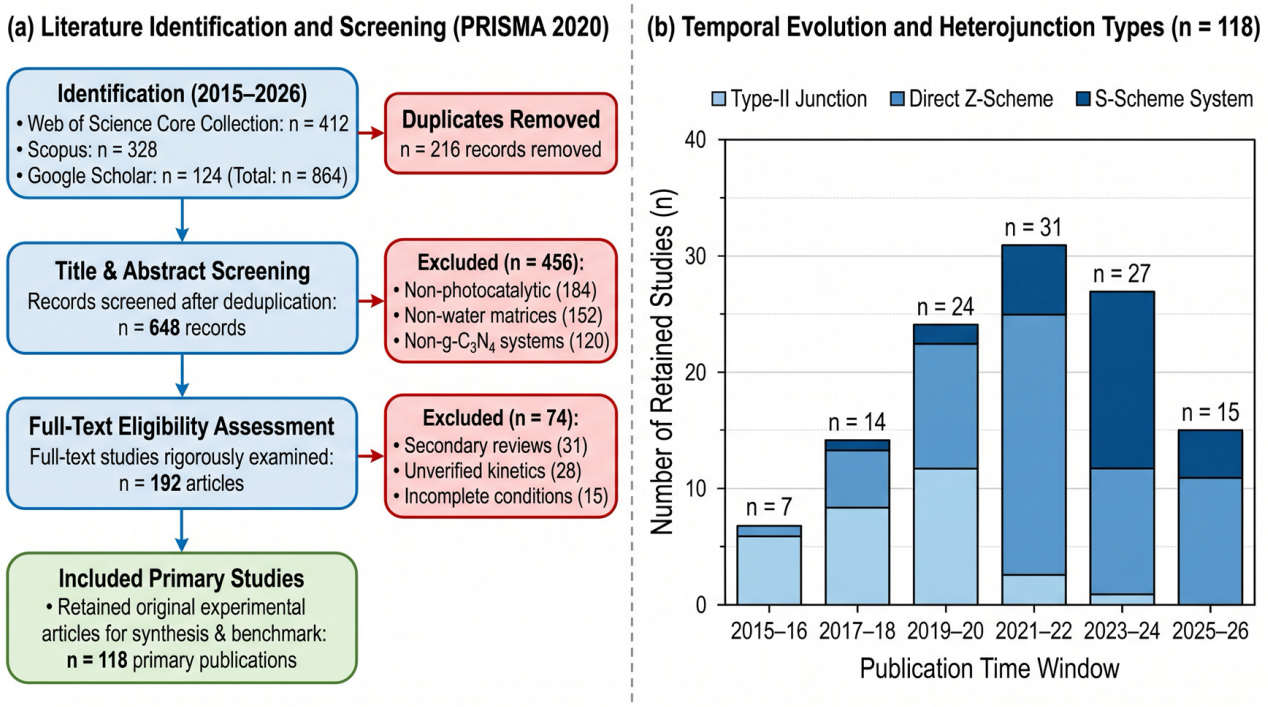



**Figure 1.** Transparent literature methodology and bibliometric distribution for g-$C_3N_4$-based heterojunctions in water remediation (2015–2026): (**a**) PRISMA 2020 flow diagram: 864 records identified (Web of Science Core Collection, 412; Scopus, 328; Google Scholar, 124), 216 duplicates removed, 648 records screened, 456 excluded (184 non-photocatalytic, 152 non-water matrices, 120 non-g-$C_3N_4$ systems), 192 full-text articles assessed, 74 excluded (31 secondary reviews, 28 unverified kinetics, 15 incomplete conditions), and 118 primary studies included; and (**b**) temporal evolution and heterojunction-configuration distribution (Type-II, direct Z-scheme, and S-scheme) across the 118 included studies.

## 2. Structure and Photocatalytic Mechanism of g-$C_3N_4$

g-$C_3N_4$ is a 2D layered non-metallic semiconductor composed of carbon and nitrogen atoms bonded via $sp^2$ hybridization to establish an extended, highly conjugated π-electron network. Its basic structural units comprise triazine ($C_3N_3$) or heptazine/tri-s-triazine ($C_6N_7$) motifs, which periodically assemble into graphite-like planar networks held together by interlayer van der Waals forces (Figure 2). g-$C_3N_4$ exhibits notable chemical and thermal stability [21]. It features a bandgap of ~2.7 eV, enabling optical absorption in the blue-edge visible region ($\lambda \leq 460$ nm). Its conduction band (CB) potential is positioned at approximately –1.1 V (vs. NHE, pH = 7), whereas the valence band (VB) edge lies at ~+1.6 V [22]. It is hereby clarified that all band-edge potentials (CB and VB) discussed in this section are normalized to pH = 7 and expressed versus the normal hydrogen electrode (NHE), unless

explicitly stated otherwise. Because band-edge positions shift with pH and measurement method, reported CB potentials of g-$C_3N_4$ span a range (approximately −1.1 to −1.63 V vs. NHE); values quoted in subsequent sections follow the conditions reported in the respective original studies (see Section 5.3) [23]. Complementary to experimental electrochemical determinations (e.g., Mott-Schottky analysis and ultraviolet photoelectron spectroscopy), density functional theory (DFT) calculations provide a powerful first-principles approach to accurately determine band edge potentials [24,25]. By constructing periodic slab models and referencing the total electrostatic potential to the absolute vacuum level ($E_{vac}$), the valence band maximum (VBM) and conduction band minimum (CBM) can be extracted directly from the projected density of states (PDOS). Given that conventional generalized gradient approximations (GGA-PBE) systematically underestimate the semiconductor bandgap, hybrid functionals (such as HSE06) or PBE+U schemes are widely implemented to correct self-interaction errors, yielding band edges and work functions that align closely with experimental values vs. NHE ($E_{NHE} = -E_{vac} - 4.44$ V at pH = 0, corrected to pH = 7 via the Nernstian shift of −0.059 V/pH). Furthermore, DFT slab calculations can resolve plane-dependent surface dipoles, work-function discrepancies, and interfacial charge redistribution, providing quantitative theoretical verification for contact-induced band bending and internal electric-field (IEF) alignment across g-$C_3N_4$ heterojunctions [26].

Under visible-light irradiation, when incident photon energy (hν) equals or exceeds the bandgap (Eg) of g-$C_3N_4$, intrinsic interband optical absorption occurs. Valence band electrons absorb photons and cross the forbidden band into the conduction band, leaving corresponding holes behind to generate photogenerated electron–hole ($e^-/h^+$) pairs [27,28]. Subsequently, photogenerated electrons and holes migrate from the bulk toward surface catalytic sites. Upon reaching the surface, CB electrons transfer to adsorbed electron acceptors (e.g., dissolved $O_2$ or $H^+$) to drive reduction reactions; dissolved oxygen is reduced to superoxide radicals ($O_2^{\bullet -}$), or high-valence metal ions (e.g., Cr(VI)) are reduced directly; simultaneously, VB holes can directly oxidize surface-adsorbed organic pollutants [29]. However, pristine g-$C_3N_4$ suffers from rapid carrier recombination, low intrinsic carrier mobility, and short diffusion lengths, causing a considerable fraction of charge carriers to recombine within the bulk or on the surface before participating in surface catalysis [30]. In addition, bulk g-$C_3N_4$ easily undergoes interlayer stacking, yielding low specific surface areas and few exposed active sites, which gives rise to mass-transfer limitations and interfacial charge-transfer resistance; its optical absorption range and surface redox kinetics also leave room for enhancement. To overcome these limitations, building g-$C_3N_4$-based heterojunctions has emerged as a primary modification strategy [31]. Coupling g-$C_3N_4$ with complementary band-matched semiconductors establishes interfacial built-in electric fields and staggered band alignments, driving photogenerated electrons and holes in opposing directions to realize spatial separation, thereby suppressing recombination and extending carrier lifetimes [32]. In addition, rational selection of narrow-bandgap components or structural tailoring synchronously expands optical absorption and multiplies accessible reaction sites [33].

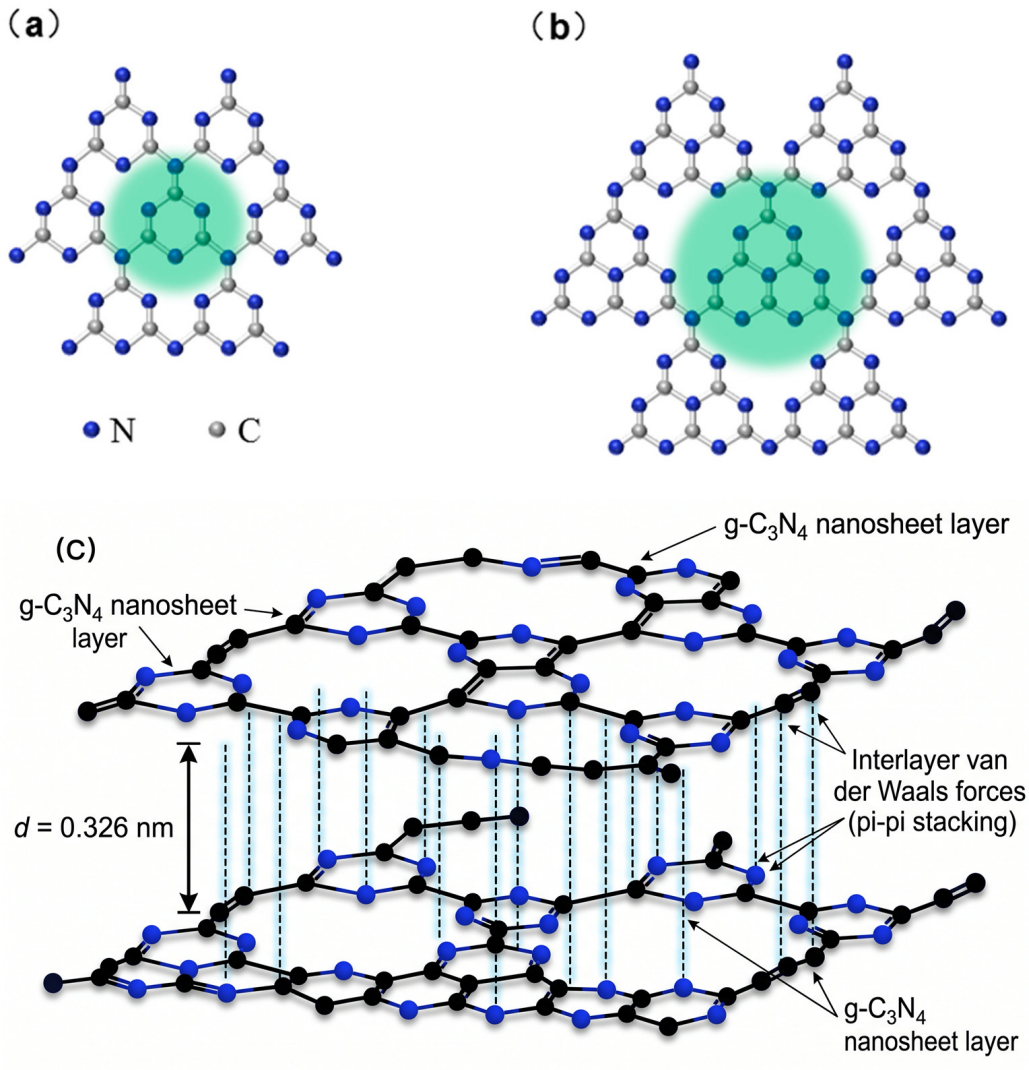



**Figure 2.** Schematic structures of g-$C_3N_4$: (**a**) triazine unit; (**b**) heptazine unit. Reproduced from Ref. [34] under CC BY 4.0 license. (**c**) 3D layered structure illustrating the interlayer distance (d ≈ 0.326 nm) and interlayer van der Waals interactions.

## 3. Main Types of g-$C_3N_4$-Based Heterojunctions

A heterojunction consists of two or more distinct semiconductor materials in intimate contact at their interface. When g-$C_3N_4$ couples with secondary semiconductors to construct heterojunctions, band alignment and interfacial contact dictate carrier migration and recombination kinetics, thereby tuning photocatalytic performance. Depending on band alignments, interfacial charge transfer directions, and carrier separation pathways, g-$C_3N_4$-based heterojunctions are classified into Type-I, Type-II, Z-scheme, and S-scheme configurations (Figure 3), where SC-I and SC-II denote Semiconductor I and Semiconductor II, respectively.

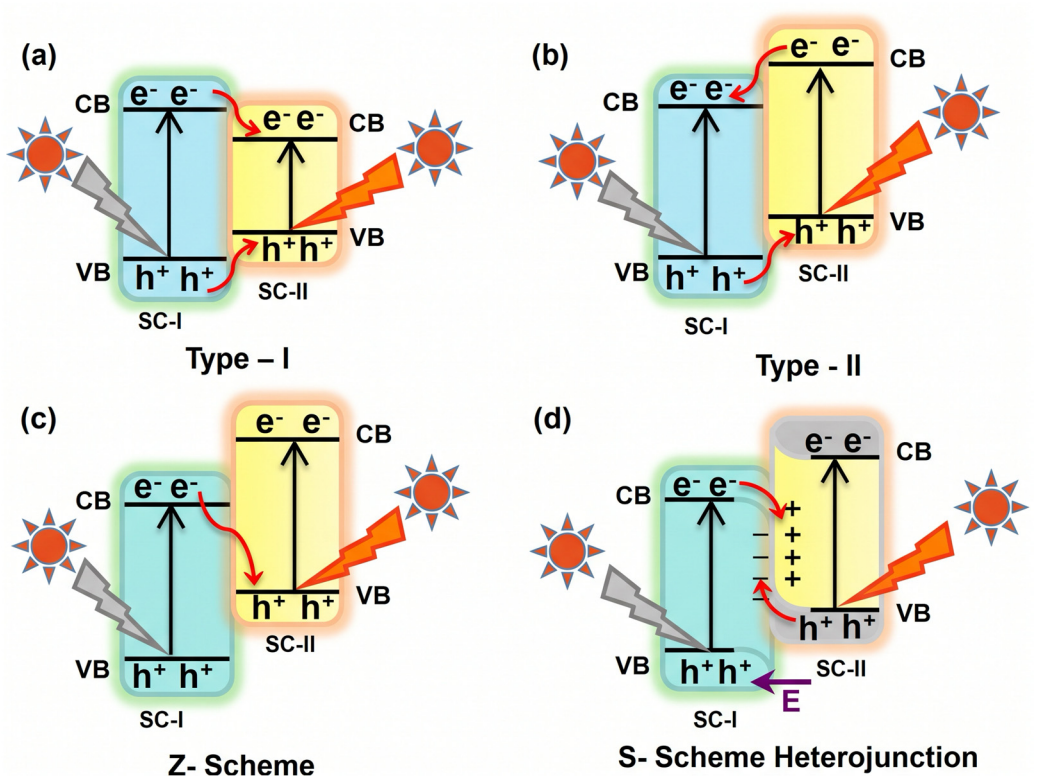



**Figure 3.** Carrier separation processes of different heterojunctions under light irradiation: (**a**) Type-I; (**b**) Type-II; (**c**) Direct Z-scheme; and (**d**) S-scheme heterojunctions. Solid black upward arrows denote photogeneration and excitation of electron–hole pairs; red curved arrows indicate charge transfer and interfacial recombination pathways; and the purple arrow represents the built-in electric field (IEF) across the interface.

### *3.1. Type-I Heterojunction*

In a Type-I heterojunction (Figure 3a), both the CB and VB edges of SC-II are located within the bandgap of SC-I, meaning SC-II exhibits a narrower bandgap. Under irradiation, both SC-I and SC-II absorb photons exceeding their bandgaps, generating CB electrons and VB holes [35]. Driven by energy level offsets, electrons in the higher-energy CB of SC-I migrate to the lower-energy CB of SC-II; concurrently, holes in the VB of SC-I transfer to the higher-energy VB of SC-II [36]. Before interfacial contact, the isolated semiconductors (SC-I and SC-II) possess distinct work functions and Fermi levels ($E_F$). Upon intimate contact, a spontaneous diffusion of electrons occurs across the interface driven by the electrochemical potential gradient until a unified Fermi level is established at thermodynamic equilibrium. This interfacial charge redistribution establishes a localized space-charge region and weak interfacial band bending. Under irradiation, despite this thermal equilibration, photogenerated electrons and holes are thermodynamically driven to accumulate on the same narrow-bandgap semiconductor owing to the straddling band offset, thereby confirming that Type-I systems fail to achieve spatial charge separation regardless of interfacial contact equilibration [37]. Consequently, both electrons and holes accumulate on SC-II (electrons gather in the CB of SC-II and holes in the VB of SC-II). Because both carrier types concentrate within the same semiconductor component, charge recombination readily occurs in the bulk or at the interface, failing to achieve effective spatial separation [38].

### *3.2. Type-II Heterojunction*

In a Type-II heterojunction (Figure 3b), the band alignments of SC-I and SC-II are staggered. Upon photoexcitation, electron–hole pairs are generated in both components [39]. Since the CB potential of SC-II is more negative (higher electron energy), photogenerated electrons in SC-II spontaneously migrate to the more positive (lower energy) CB of SC-I; simultaneously, photogenerated holes on the more positive VB of SC-I transfer to the more negative (higher energy) VB of SC-II [40]. In conventional discussions of Type-II heterojunctions, energy levels are frequently depicted using simplified flat-band alignments. Before contact, SC-I and SC-II feature staggered band edges with different Fermi levels. Upon physical contact, free electrons migrate from the component with the higher Fermi level (lower work function) to that with the lower Fermi level, creating an interfacial internal electric field (IEF) and inducing upward/downward band bending at the junction boundary. Steady-state photogenerated electrons in the higher CB transfer to the lower CB, while holes migrate in the opposite direction. Explicitly acknowledging this contact-induced band bending clarifies that the bidirectional migration in Type-II junctions operates in competition with the interfacial barrier, which partially accounts for the thermodynamic driving force loss commonly observed in real systems [41].

Consequently, photogenerated electrons collect on the CB of SC-I, whereas holes accumulate on the VB of SC-II. Therefore, Type-II heterojunctions retain electrons with a weaker reduction potential on SC-I and holes with a weaker oxidation potential on SC-II, representing an inherent thermodynamic limitation [42]. Before contact, isolated SC-I and SC-II exhibit independent band edges and work functions. Upon intimate interfacial contact, spontaneous electron transfer occurs driven by the Fermi-level difference until equilibrium is established at the interface, generating band bending and an interfacial contact barrier. Under subsequent illumination, photogenerated electrons slide down the staggered conduction band offset, while holes transfer along the valence band gradient.

### *3.3. Z-Scheme Heterojunction*

In an all-solid-state direct Z-scheme heterojunction (Figure 3c), the semiconductor with deeper band positions (e.g., BiOBr, $Fe_2O_3$) is typically denoted as SC-I, while the more negative component (e.g., g-$C_3N_4$) is designated as SC-II [43]. As systematically formulated by Low et al. [37] in an all-solid-state direct Z-scheme heterojunction, staggered band alignment is retained while inactive carriers undergo interfacial recombination, thereby preserving strong redox overpotentials on the outer band edges. Under visible illumination, both components are excited to generate electron–hole pairs. Subsequently, photogenerated electrons with weaker reduction ability in the CB of SC-I migrate toward the interface and recombine rapidly with photogenerated holes with weaker oxidation ability in the VB of SC-II [44]. Through this directional recombination process, high-energy electrons ($e^-$) with strong reduction potential are preserved in the CB of SC-II, migrating to the surface to drive $O_2^{\bullet-}$ formation or participate directly in reductive dehalogenation/defluorination [45]; simultaneously, deep-energy holes ($h^+$) with strong oxidation capacity remain in the VB of SC-I to directly oxidize organics or generate ·OH for deep ring-cleavage reactions [46–48]. Before contact, the two semiconductors exhibit staggered band structures. Following interfacial contact, charge redistribution forces their respective Fermi levels into alignment, generating localized band bending and an interfacial contact barrier. Concurrently, the accumulated charge density and localized interface states at the junction facilitate the quasi-ohmic recombination of relatively low-potential electrons from the CB of SC-I with low-potential holes from the VB of SC-II. Consequently, the highly reductive electrons in SC-II and strongly oxidative holes in SC-I are preserved at the outer spatial regions, resolving the apparent thermodynamic paradox [49]. This pathway integrates efficient spatial carrier

separation with the maximum preservation of high redox potentials, cleverly overcoming the intrinsic thermodynamic sacrifice of traditional Type-II heterojunctions [50–52].

### *3.4. S-Scheme (Step-Scheme) Heterojunction*

An S-scheme heterojunction (Figure 3d), first introduced by Fu et al. [53] to describe directional charge transfer between an oxidation photocatalyst (OP) and a reduction photocatalyst (RP) with staggered band alignment, represents a conceptual evolution beyond the traditional Z-scheme model [54]. In the dark, electrons spontaneously diffuse from SC-II to SC-I until Fermi levels equilibrate [55], causing SC-II to become positively charged and SC-I negatively charged [56]. This forms an interfacial built-in electric field (IEF) directed from SC-II toward SC-I and drives downward band bending in SC-I alongside upward band bending in SC-II [57,58]. Under photoexcitation, the synergy of the IEF, band bending potential barriers, and Coulombic attraction drives electrons with lower reduction potential in the CB of SC-I to recombine preferentially with lower-oxidation-potential holes in the VB of SC-II at the interface [59,60]; meanwhile, highly reductive high-energy electrons and highly oxidative high-energy holes are preserved in the CB of SC-II (RP) and the VB of SC-I (OP), respectively [61]. This mechanism accomplishes efficient spatial carrier separation while maximally maintaining the robust redox overpotentials of the system.

### *3.5. Experimental Criteria for Verifying Heterojunction Charge-Transfer Pathways*

Mechanistic assignments of type-II, Z-scheme, and S-scheme pathways should not rest on thermodynamic band-alignment estimates alone, as staggered band structures are compatible with multiple charge-transfer routes. A robust assignment generally combines several complementary experiments: (i) band-edge and Fermi-level determination, using valence-band XPS or ultraviolet photoelectron spectroscopy together with Mott–Schottky analysis and UV–vis diffuse reflectance, to establish band positions and work functions of both components before and after contact [62]; (ii) Kelvin probe force microscopy or surface photovoltage measurements, which map interfacial potential differences and the direction of the built-in electric field [63]; (iii) in situ irradiated XPS, in which light-induced binding-energy shifts monitor interfacial electron redistribution; however, such shifts should not be treated as a stand-alone direct proof of an S-scheme mechanism due to potential surface photovoltage artifacts or differential charging. A definitive assignment requires cross-validation with work-function/Fermi-level alignments (UPS/Kelvin probe), built-in electric field direction (SPV/KPFM), and time-resolved carrier-lifetime dynamics [64]; (iv) time-resolved spectroscopy, such as femtosecond transient absorption and time-resolved photoluminescence, which resolves carrier lifetimes and interfacial transfer kinetics [65]; and (v) reactive-species profiling, combining electron paramagnetic resonance spin trapping, radical-quenching experiments, and probe-molecule assays, to verify that the redox products actually formed are thermodynamically consistent with the proposed pathway [66]. Cross-validation with at least two independent techniques is recommended before a charge-transfer mechanism is claimed.

## 4. Preparation Methods of g-$C_3N_4$-Based Heterojunctions

Two primary factors govern the catalytic efficiency of carbon nitride heterojunctions: selecting secondary semiconductors with suitable band matching to govern carrier migration and maintain redox capacity, and employing effective heterojunction construction methods. Protocols including chemical vapor deposition, hydrothermal/solvothermal methods, high-temperature calcination, sol–gel processing, in situ polymerization and deposition–precipitation and electrostatic/ultrasonication assembly and photodeposition

have been successfully utilized [67], a comprehensive comparison of which is summarized in Table 1.

### *4.1. Chemical Vapor Deposition (CVD)*

Chemical vapor deposition vaporizes solid or liquid precursors at elevated temperatures and transports the vapor phase via carrier gases into a high-temperature reaction zone, where decomposition, reaction, or polymerization occurs on substrate surfaces to yield thin-film materials. Under an inert atmosphere at elevated temperatures, vaporized organic precursors condense and polymerize in situ onto substrates or pre-synthesized g-$C_3N_4$ surfaces, facilitating the conformal growth of secondary semiconductors with atomic-scale interfacial bonding [68,69]. Chubenko et al. [70] reported g-$C_3N_4$ films grown by chemical vapor deposition on various substrates, providing a scalable route to uniform coatings. CVD represents a primary route for producing g-$C_3N_4$-based heterojunction films with high crystallinity, clean interfaces, and structural continuity [71].

### *4.2. Hydrothermal/Solvothermal Method*

Hydrothermal and solvothermal methods are widely used to construct g-$C_3N_4$-based heterojunctions under relatively mild conditions—typically at operational temperatures of 120–200 °C and autogenous pressures below 2 MPa within sealed Teflon-lined autoclaves—compared to conventional high-temperature solid-state calcination (>500 °C). A representative case is the in situ hydrothermal growth of a g-$C_3N_4$–$Bi_2O_3$ heterojunction at 180 °C for 12 h in a Teflon-lined autoclave, in which the optimized composite degraded 93% of tetracycline hydrochloride within 90 min under UV-A irradiation [72]. These sealed, subcritical liquid environments enable precise control over crystallite nucleation, facet exposure, and intimate interfacial contact while preserving the thermal integrity of the polymeric melon network [73,74]. Moreover, by optimizing reaction temperatures and solvent properties, hydrothermal/solvothermal routes promote highly dispersed, intimate anchoring of metal oxides and other semiconductors across g-$C_3N_4$, exposing additional active sites while enhancing interfacial charge transfer efficiency [75].

### *4.3. High-Temperature Calcination*

High-temperature calcination, also termed thermal polycondensation, involves blending g-$C_3N_4$ molecular precursors with secondary semiconductor precursors, followed by high-temperature processing [76]. During heating, nitrogen-rich precursors undergo deamination and condensation into g-$C_3N_4$, while the secondary component undergoes decomposition, oxidation, sulfidation, or crystallization, yielding the heterojunction in a single step. Compared to multi-step post-assembly routes, this method establishes stronger interfacial chemical bonding [77]. Zhang et al. [78] prepared a $TiO_2$/g-$C_3N_4$ heterojunction by in situ growth of $TiO_2$ nanocrystals on g-$C_3N_4$ nanosheets through an impregnation–calcination route, which produced intimate interfacial contact and enhanced charge separation. Thermal condensation of pure g-$C_3N_4$ typically occurs between 500 and 600 °C in covered alumina crucibles under air or inert gas at heating rates of 2–10 °C·$min^{-1}$ for 2–4 h [79]. Excess secondary phases can lead to particle agglomeration or bury active sites, requiring careful optimization of precursor ratios, temperatures, and heating rates [80].

### *4.4. Sol–Gel Method*

The sol–gel approach uses metal alkoxides or inorganic salts as precursors to form a uniform colloidal sol via hydrolysis and condensation, which transitions into a gel and converts to composite semiconductors after drying and heat treatment [81]. Its core advantage lies in achieving uniform mixing at molecular or nanoscale levels. Exfoliated g-$C_3N_4$ nanosheets are dispersed in an alcohol–water matrix to guide controlled hydrolysis and con-

densation of metal precursors across the sheets, forming core–shell or anchored heterostructures [82–84]. Zhang et al. [85] prepared g-$C_3N_4$/$TiO_2$ heterostructured nanocomposites via a modified sol–gel route coupled with calcination. By slowly hydrolyzing tetrabutyl titanate in an ethanolic suspension containing exfoliated g-$C_3N_4$, ultrafine $TiO_2$ nanoparticles were uniformly anchored onto g-$C_3N_4$ surfaces, markedly boosting specific surface area and interfacial charge separation while conferring superior activity and stability.

### *4.5. In Situ Polymerization and Deposition–Precipitation*

In situ polymerization involves introducing pre-synthesized secondary semiconductors, coordination complexes, or monomer precursors directly into the polycondensation stage of carbon nitride precursors (e.g., urea, thiourea, melamine, or dicyandiamide) [86,87]. Under thermal treatment, the volatilized or condensing molecular precursors polymerize directly across the surface of the embedded guest components, forming an interpenetrated, tightly wrapped hybrid network [88,89]. This strategy avoids the macroscopic phase segregation and interfacial cracking often encountered during post-synthesis mechanical mixing, effectively establishing atomically intimate contact and extended pi-conjugated interfacial pathways that facilitate rapid charge transfer [90,91]. Deposition–precipitation utilizes wet-chemical precipitation to anchor secondary nanoparticles onto dispersed g-$C_3N_4$ nanosheets [92]. A precipitating agent (e.g., NaOH, $NH_4OH$, or in situ urea hydrolysis) is slowly introduced into an aqueous suspension containing exfoliated g-$C_3N_4$ and metal cations under continuous stirring, driving the controlled, homogeneous nucleation and deposition of insoluble metal hydroxides or basic carbonates onto g-$C_3N_4$ active sites [93,94]. Subsequent low-temperature washing and mild calcination convert the precipitates into well-crystallized metal oxide or sulfide nanoparticles with high surface dispersion, minimizing severe nanoparticle self-aggregation [95,96].

### *4.6. Electrostatic/Ultrasonication Assembly and Photodeposition*

Electrostatic and ultrasonication-assisted assembly is a facile, non-destructive physical assembly method governed by surface charge matching [97,98]. Because exfoliated g-$C_3N_4$ nanosheets typically possess negative surface zeta potentials across a wide pH range, they can spontaneously electrostatically assemble with positively charged secondary nanomaterials (e.g., layered double hydroxides, Bi-based oxyhalides, or modified metal oxides) in aqueous media under ultrasonic dispersion [99,100]. High-intensity ultrasound generates localized acoustic cavitation, promoting high-speed microjets that facilitate intimate 2D/2D facial contact without destroying the intrinsic crystal lattices or exposed reactive facets of the parent materials [101,102]. Photodeposition is an in situ, light-driven chemical assembly route conducted at ambient temperature [103]. Under visible or UV light irradiation, photogenerated electrons or holes that migrate to the g-$C_3N_4$ surface selectively reduce metal ions (e.g., $Ag^+$, $Pt^{4+}$, $Au^{3+}$, $Pd^{2+}$) into metallic nanoparticles or oxidize metal ions (e.g., $Mn^{2+}$, $Co^{2+}$) into metal oxides [104,105]. Because the growth of the secondary phase occurs strictly at the photogenerated charge accumulation sites, photodeposition yields precise, facet-selective nanoscale heterojunctions with minimal interfacial defects and low energy consumption [106,107].

**Table 1.** Comprehensive comparison of mainstream and emerging fabrication strategies for g-$C_3N_4$-based heterojunctions.

| Fabrication Route | Typical Conditions (Temp./Pressure) | Interfacial Bonding Nature | Morphology Control | Energy Demand | Scalability | Key Advantages | Major Limitations | Ref. |
|---|---|---|---|---|---|---|---|---|
| Chemical Vapor Deposition (CVD) | 500–650 °C; inert atmosphere or vacuum | Atomic-scale, continuous, pinhole-free contact | High (uniform conformal thin films) | High | Moderate | Clean interface, minimal defects, superior structural stability | High equipment cost; low yield for bulk powdered photocatalysts | [70] |
| Hydrothermal/ Solvothermal | 120–200 °C; 0.2–2 MPa (autogenous) | Strong chemical coordination/covalent bonds | High (in situ vertical nucleation and growth) | Moderate | High | Intimate interfacial contact, tailored crystal facets, high dispersion | Uses organic solvents; autoclave volume and safety limits | [72] |
| High-Temperature Calcination | 500–550 °C; air or inert gas | Robust covalent/metalloid interfacial bonds | Moderate (risk of thermal sintering) | High | Very high | Simple one-step route, solvent-free, highly scalable | Thermal agglomeration; potential burial of surface active sites | [78,79] |
| Sol–Gel Method | 25–100 °C (followed by mild annealing) | Molecular-level anchorages and coordination | High (core–shell or nano-anchored structures) | Moderate | High | Uniform precursor dispersion, high specific surface area | Susceptible to cracking during drying; requires multi-step calcination | [82–85] |
| In Situ Polymerization | 80–180 °C; wet/hydrothermal conditions | Interpenetrated π-conjugated network | Good (intercalated or wrapped architectures) | Low to moderate | High | Prevents phase segregation; preserves exposed active facets | Unreacted precursor residues require rigorous extraction | [88,91] |
| Electrostatic/ Ultrasonication Assembly | Room temperature (20–50 °C); ambient pressure | Interfacial Coulombic forces and van der Waals | Moderate (governed by precursor morphology) | Very low | High | Facile, green, room-temperature operation, non-destructive | Weaker interfacial binding; risk of particle detachment in continuous flow | [101,102] |
| Photodeposition | 20–40 °C; ambient pressure under light | Selective facet-dependent deposition | High (targeted localized nanoparticle loading) | Low | Moderate | Room-temperature, site-selective co-catalyst anchoring | Restricted to light-reducible or light-oxidizable metal ions | [104,106] |

## 5. Applications of g-$C_3N_4$ Heterojunctions in Water Purification

Through band-alignment engineering and accelerated charge-carrier separation, g-$C_3N_4$-based heterojunctions resolve key limitations of pristine g-$C_3N_4$, including rapid carrier recombination, inadequate redox potentials, and restricted visible-light absorption. Recent progress in photocatalytic water purification is reviewed below across emerging contaminant degradation, pathogenic microbial inactivation, and high-valence heavy metal reduction [108]. To offer a comprehensive perspective, representative g-C3N4-based heterojunction photocatalytic systems across these three water purification domains—including their heterojunction types, primary reactive species, operational parameters, and target pollutant removal efficiencies—are systematically summarized in Table 2.

### *5.1. Degradation of Emerging Contaminants*

Emerging aquatic contaminants, such as microplastics (MPs), antibiotics, persistent organic pollutants (POPs), and endocrine-disrupting chemicals (EDCs), exhibit persistent environmental resistance and high ecotoxicity [109–111]. Constructing g-$C_3N_4$-based heterojunctions synergistically enhances adsorption capacity and carrier dynamics, supplying

conduction-band electrons and reactive oxygen species (ROS) to drive dehalogenation, aromatic ring opening, and thorough mineralization. Pristine g-$C_3N_4$ displays limited activity toward recalcitrant microplastics, typically yielding mass loss below 15% without measurable mineralization. In evaluating microplastic removal, it is imperative to clearly delineate physical adsorption, mechanical fragmentation, surface oxidation, macromolecular chain scission, mass loss, and authentic TOC mineralization to avoid overestimating degradation efficacy. For instance, physical adsorption concentrates microplastics onto the catalyst surface, whereas true photocatalytic destruction is initiated by reactive radical attack on polymer backbones, inducing oxygen-containing functional groups (C–O, C=O), successive chain scission into short-chain oligomers, and ultimate mineralization into $CO_2$ and $H_2O$ [112,113]. Nguyen et al. [114] synthesized a $TiO_2$-modified UiO-66/g-$C_3N_4$ heterojunction from terephthalic acid recovered from waste PET, which achieved up to 90% visible-light degradation of polystyrene microplastics within 30 h; electrochemical impedance spectroscopy confirmed efficient interfacial charge transfer. Jia et al. [115] fabricated oxygen-vacancy-rich $MoO_{3-x}$/g-$C_3N_4$ Z-scheme heterojunctions, achieving 97% degradation under continuous visible illumination for 7 days, whereas pristine g-$C_3N_4$ remained largely inactive. The heterojunction exhibited superior carrier separation and transport kinetics; its direct Z-scheme alignment was strictly substantiated by in situ irradiated XPS (displaying binding energy shifts of Mo 3d and C 1s toward opposite directions under light) and DMPO-trapping EPR, which confirmed the simultaneous generation of both $O_2^{\bullet-}$ and ·OH without sacrificial hole consumption while preserving high redox overpotentials. Lu et al. [116] designed a direct Z-scheme g-$C_3N_4$/$WO_3$ nanocomposite, achieving a 93.3% photodegradation of tetracycline hydrochloride (TC-HCl) under visible light with an apparent reaction rate constant ($k$ = 0.0142 $min^{-1}$) substantially surpassing pristine counterparts (Figure 4a). The transient photocurrent responses (Figure 4b) revealed a substantially stronger photocurrent for the g-$C_3N_4$/$WO_3$ heterojunction than for pristine g-$C_3N_4$ and pure $WO_3$, indicating more efficient separation and interfacial transfer of photogenerated electron-hole pairs. Crucially, spin-trapping ESR spectra explicitly resolved the concurrent evolution of robust DMPO-$O_2^{\bullet-}$ and DMPO-··OH signals under irradiation. Because the single-phase band potentials of $WO_3$ conduction band and g-$C_3N_4$ valence band are thermodynamically incapable of directly yielding $O_2^{\bullet-}$ and ·OH, respectively, this dual-ROS generation provided unequivocal spectroscopic verification for the direct Z-scheme charge-transfer pathway (Figure 4c), which spatially segregates reactive carriers while preserving high redox overpotentials. Electron paramagnetic resonance (EPR) spin trapping and radical scavenging assays confirmed that high concentrations of photogenerated $O_2^{\bullet-}$ and ·OH drove the oxidative cleavage, while liquid chromatography–mass spectrometry (LC–MS) tracked the transformation intermediates, confirming the sequential breakdown of macromolecular chains and final detoxification.

Heterojunction architectures demonstrate outstanding efficiency in antibiotic mineralization and antibiotic resistance gene (ARG) disruption [117,118]. Zheng et al. [119] prepared a g-$C_3N_4$/$Cr_2O_3$ composite governed by an S-scheme charge transfer mechanism, retaining high-reduction electrons in the g-$C_3N_4$ CB and high-oxidation holes in the $Cr_2O_3$ VB. Under this synergy, 63.8% of tetracycline TOC mineralization was achieved within 50 min, with a rate constant 2.6 times that of pristine g-$C_3N_4$. For POPs with high bond energies (e.g., C–F and C–Cl bonds), heterojunctions continuously supply energetic electrons and ROS to drive deep dehalogenation and mineralization. Parallel efforts tackling POPs have focused on per- and polyfluoroalkyl substances (PFAS), where the exceptional bond dissociation energy of C–F linkages (~485 kJ/mol) resists conventional degradation pathways. Navidpour et al. [120] constructed a ZnO@citric acid-modified g-$C_3N_4$ hybrid catalyst capable of accelerated perfluorooctanoic acid (PFOA) elimination (Figure 4d). The

optimized 5 wt% hybrid exhibited an apparent rate constant of 0.468 $h^{-1}$ under UV light (a 4.8-fold improvement over ball-milled ZnO), which was further elevated to 0.868 $h^{-1}$ upon peroxymonosulfate (PMS) activation (Figure 4e); Scavenger quenching assays and charge-transfer modeling confirmed that photogenerated holes ($h^+$) alongside derived $O_2^{\bullet-}$ and $SO_4^{\bullet-}$ radicals trigger primary Kolbe decarboxylation ($C_7F_{15}COO^- \rightarrow C_7F^{\bullet}_{15} + CO_2$), subsequently initiating sequential chain-shortening cycles that drive comprehensive defluorination into fluoride ions and $CO_2$ (Figure 4f). Kang et al. [121] synthesized an oxygen-vacancy-rich direct Z-scheme g-$C_3N_4$/BiOBr heterojunction via a PVP-assisted solvothermal approach. The optimal composite (CN/VoBOB-15, 15 wt% g-$C_3N_4$) achieved 93% RhB and 91% Congo red degradation within 30 min under LED irradiation, yielding an apparent rate constant ($k$ = 0.07667 $min^{-1}$ for RhB) that was 57.6 and 6.7 times higher than those of pristine g-$C_3N_4$ and vacancy-rich BiOBr, respectively. Active-species trapping and DFT work-function evaluations confirmed a direct Z-scheme charge-transfer mechanism, driven by synergistic carrier separation and retained strong redox overpotentials ($O_2^{\bullet-}$ and $h^+$ dominant). When treating EDCs containing stable aromatic structures and phenolic groups [122,123], complex water matrices demand elevated catalytic durability. Duan et al. [124] fabricated an intimate 2D/2D direct Z-scheme g-$C_3N_4$/$Bi_2O_2CO_3$/porous g-$C_3N_4$ heterojunction via a two-stage template-free route. The optimized composite with 2 wt% $Bi_2O_2CO_3$ exhibited a pseudo-first-order rate constant of $k$ = 0.0608 $min^{-1}$ toward tetracycline hydrochloride under simulated sunlight, which was 5.1 times higher than that of porous g-$C_3N_4$ nanosheets, achieving 97.4% degradation within 60 min with robust stability over five consecutive cycles. Masekela et al. [125] reviewed MXene-based nanocomposites for photocatalytic wastewater treatment, $CO_2$ reduction, and $H_2$ production, highlighting g-$C_3N_4$/MXene heterojunctions as a promising family for enhanced charge separation. Zhao et al. [126] developed a Bi-based ternary heterojunction that maintained over 78% degradation efficiency in complex real water matrices, demonstrating practical application potential. In addition to refractory antibiotics and emerging POPs, classic organic dye degradation remains an essential benchmark for evaluating carrier transfer efficiency. Dai et al. [127] constructed a 5 wt% $Co_3O_4$/g-$C_3N_4$ Type-II heterojunction via coupled hydrothermal and calcination methods. Driven by the staggered band alignment, photogenerated electrons accumulated on the g-$C_3N_4$ conduction band while holes were steered to the $Co_3O_4$ valence band, delivering a Rhodamine B (RhB) degradation rate of 97.6% within 40 min under simulated solar light ($k$ = 0.0703 $min^{-1}$, 2.93- and 5.58-fold higher than pristine g-$C_3N_4$ and pure $Co_3O_4$, respectively). Active species trapping and ESR spin-trapping confirmed that $O_2^{\bullet-}$ and $h^+$ served as the dominant reactive entities governing the photooxidation process. A comparative appraisal across the heterojunction categories reveals that while Type-II systems provide directional electron/hole separation, their photocatalytic redox driving forces are inherently compromised because electrons and holes migrate to thermodynamically weaker levels. In contrast, all-solid-state direct Z-scheme and S-scheme configurations preserve uncompromised redox potentials (e.g., highly negative CB electrons for $O_2^{\bullet-}$ generation and deep VB holes for ·OH evolution), yielding noticeably superior mineralization rates ($k$ values several-fold higher—typically 2–5-fold among the studies summarized here) and deeper dehalogenation capability toward refractory contaminants such as microplastics. From a practical water-treatment perspective, the presence of natural organic matter (NOM) in authentic surface waters inevitably induces active-site competition and light attenuation, while coexisting anions ($HCO_3^-$, $Cl^-$, $SO_4^{2-}$) act as scavenger sinks for ·OH and $h^+$, frequently resulting in lower reaction rates than in deionized water (commonly by ~15–30% in the cited studies).

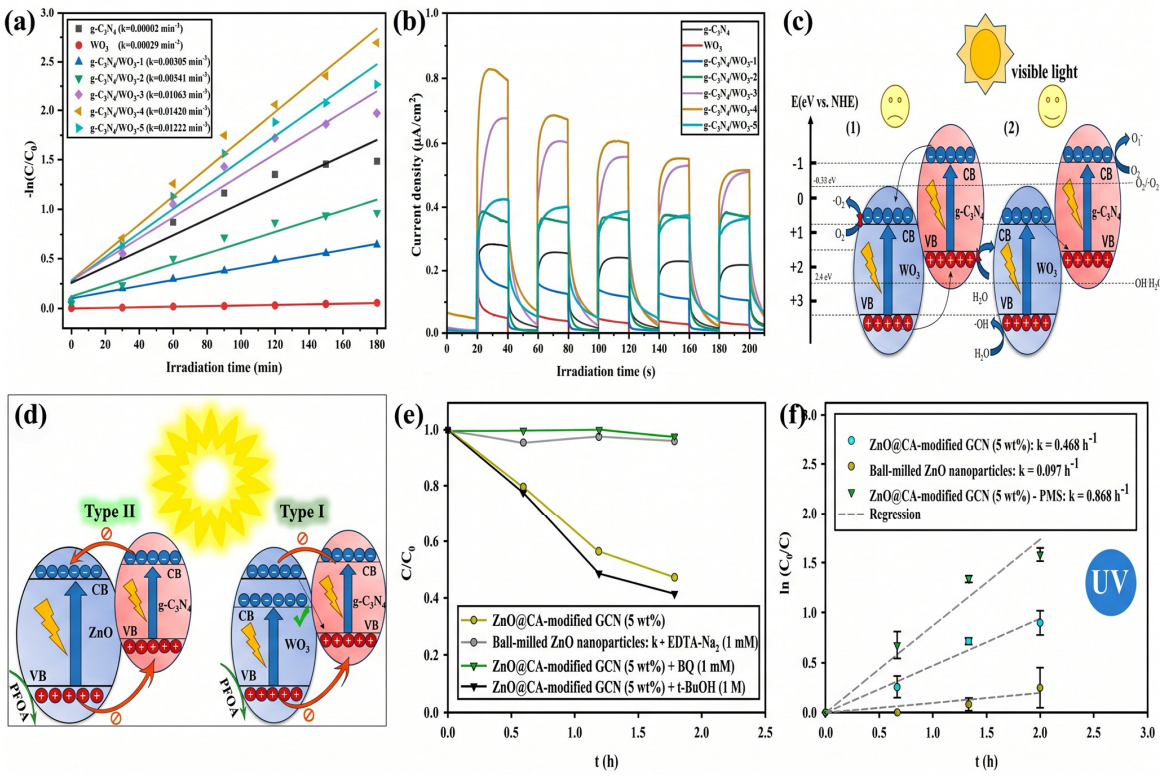



**Figure 4.** Photocatalytic degradation performance, interfacial charge transfer and mechanism validation of g-$C_3N_4$-based heterojunctions. (**a**) Pseudo-first-order kinetic plots of pollutant degradation over g-$C_3N_4$/$WO_3$ composites with different mass ratios; (**b**) transient photocurrent responses of pristine g-$C_3N_4$, pure $WO_3$ and g-$C_3N_4$/$WO_3$ heterojunctions; and (**c**) schematic illustration of charge migration pathways and reactive oxygen species generation over the g-$C_3N_4$/$WO_3$ heterojunction under visible light. Reproduced from Ref. [116] under CC BY 4.0 license; (**d**) Schematic illustration comparing the charge transfer mechanisms of Type-II and Type-I heterojunctions construct-ed from ZnO and N-vacancy-rich CA-modified GCN under light irradiation. Green arrows with checkmarks (✔) denote the thermodynamically favored charge transfer pathways and the PFOA degradation routes driven by pho-togenerated holes. Orange curved arrows accompanied by red prohibition signs (⊘) indicate the thermodynamically unfavorable or obstructed pathways. The labels $e^-$ and $h^+$ represent photogenerated electrons and holes in the re-spective conduction and valence bands; (**e**) effects of different radical scavengers on the photocatalytic activity of ZnO@CA-modified g-$C_3N_4$; and (**f**) kinetic comparison of pollutant degradation over different catalytic systems under UV irradiation. Reproduced from Ref. [120] under CC BY 4.0 license.

### *5.2. Inactivation of Pathogenic Microorganisms*

Pathogenic microorganisms in aquatic environments, including Gram-positive/negative bacteria, viruses, fungi, and algae, induce infectious diseases and threaten public health. Chlorination can form hazardous halogenated disinfection byproducts, while ultraviolet (UV) treatment is subject to high energy consumption, light attenuation from turbidity, and bacterial photoreactivation, offering limited efficacy toward resistant species [128]. Forming intimate heterojunction interfaces redirects carrier transport and curbs electron–hole recombination, generating higher yields of reactive species including $h^+$, $O_2^{\bullet-}$, ·OH and $^1O_2$. These active species attack bacterial cell walls, membranes, peripheral proteins, intracellular enzymes, and nucleic acids, causing membrane permeabilization, cytoplasmic leakage, metabolic cessation, and irreversible DNA/RNA oxidation, thereby realizing multi-target disinfection. For instance, Zhan et al. [129] engineered an AgBr/g-$C_3N_4$ direct Z-scheme heterojunction that achieved complete visible-light inactivation of $10^7$ CFU/mL *E. coli* within 90 min. The Z-scheme preserves the strongly reducing electrons of g-$C_3N_4$ and the

strongly oxidizing holes of AgBr, sustaining the concurrent generation of $O_2^{\bullet-}$ and ·OH, although natural organic matter (>0.5 mg/L) attenuates the disinfection efficiency. Beyond chemical radical oxidation, Zhang et al. [130] developed a metal-free UCN/RGO/SCN homojunction demonstrating broad-spectrum bactericidal efficiency (>99.8% against both *E. coli* and *S. aureus*) under visible-light irradiation (λ > 400 nm). The sharp edges of the embedded RGO physically pierced and disrupted bacterial cell envelopes, while the dual carbon nitride homojunction suppressed charge-carrier recombination to sustain elevated yields of reactive $O_2^{\bullet-}$ and ·OH species.

In contrast to systems driven by diffused radicals, Chen et al. [131] synthesized ordered mesoporous g-$C_3N_4$ (omg-$C_3N_4$) using SBA-15 as a hard template, and SEM/TEM images show a worm-like morphology with hexagonally arranged mesopores (Figure 5a). The ordered mesoporous framework improves light harvesting and charge separation, as reflected in the substantially stronger transient photocurrent of omg-$C_3N_4$ than that of bulk g-$C_3N_4$ (B-$C_3N_4$) under repeated on–off illumination (Figure 5b). Accordingly, omg-$C_3N_4$ produced a much faster decline in bacterial survival than B-$C_3N_4$, the dark control, and the catalyst-free control (Figure 5c). Zhang et al. [132] further showed that the disinfection performance of a nanowired g-$C_3N_4$ film depends on the precursor mass used in the vapor-assisted confined deposition: at a fixed melamine:urea ratio of 3:1, the 50 mg sample outperformed the 30 and 100 mg samples (Figure 5d), while hydrophobic modification strongly suppressed inactivation relative to the superhydrophilic film (Figure 5e). Scavenger-quenching experiments identified $H_2O_2$ as the dominant reactive species (Figure 5f), indicating that $H_2O_2$, rather than ·OH, $O_2^{\bullet-}$ or $h^+$, drives the antibacterial action. In real disinfection systems, elevated water turbidity and bacterial aggregation impede photon penetration, while residual cellular fragments can foul catalyst interfaces. Establishing long-term bactericidal durability and confirming the absence of bacterial photoreactivation under ambient light post-treatment are vital for engineering applications.

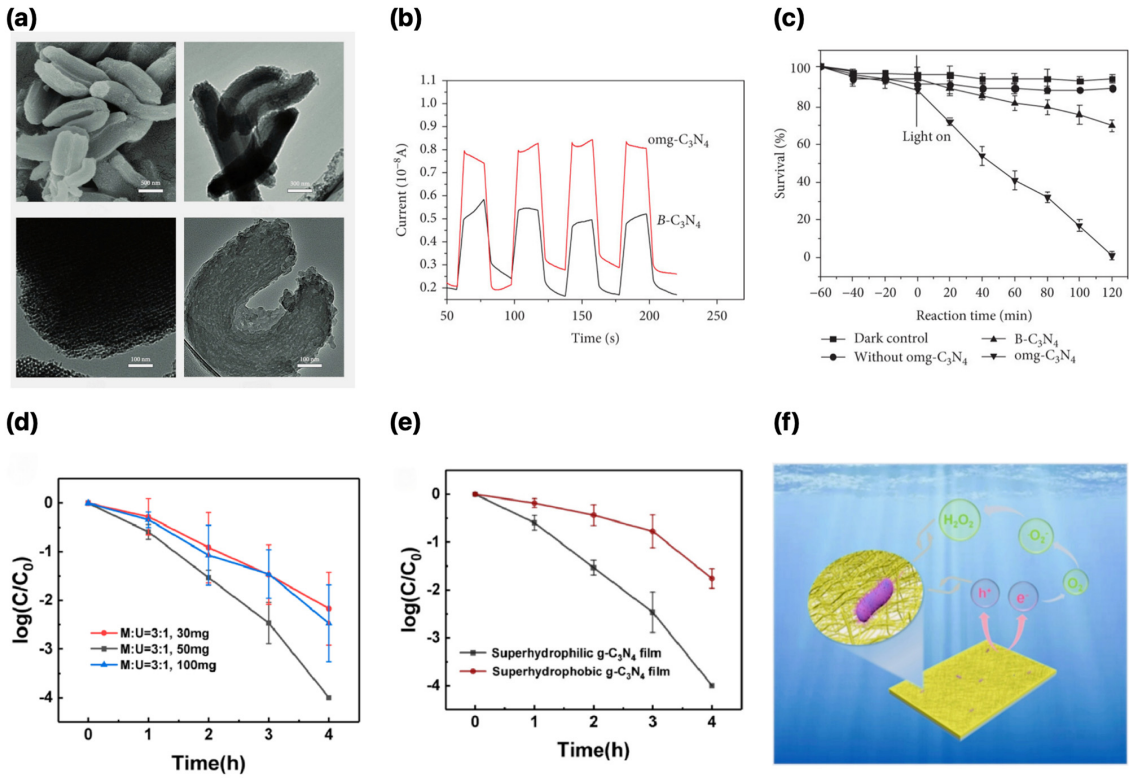



**Figure 5.** Visible-light-driven photocatalytic bacterial disinfection performance and mechanistic validation of g-$C_3N_4$-based photocatalysts: (**a**) SEM and TEM images of ordered mesoporous

g-$C_3N_4$ (omg-$C_3N_4$); (**b**) transient photocurrent responses of omg-$C_3N_4$ and bulk g-$C_3N_4$ (B-$C_3N_4$) under repeated on–off visible-light illumination; and (**c**) bacterial survival curves obtained with omg-$C_3N_4$, B-$C_3N_4$, under dark conditions, and without catalyst. Reproduced from Ref. [131] under CC BY 4.0 license; (**d**) inactivation kinetics over g-$C_3N_4$ films prepared with different precursor masses (melamine:urea = 3:1; 30, 50 and 100 mg); (**e**) effect of surface wettability (superhydrophilic versus superhydrophobic film) on the disinfection performance; and (**f**) Schematic illustration of the proposed photocatalytic bacterial inactivation and reactive oxygen species (ROS) gen-eration mechanism over the catalytic film under light irradiation. Reproduced from Ref. [132] under CC BY 4.0 license.

### *5.3. Reduction of High-Valence Heavy Metal Ions*

Industrial effluents often contain toxic and persistent heavy metals and radionuclides, including chromium Cr(VI), mercury Hg(II), and uranium U(VI) [133]. Conventional precipitation and adsorption approaches frequently suffer from excessive sludge generation and poor trace-level sequestration [134]. Heterojunction systems based on g-$C_3N_4$ exploit energetic conduction-band electrons to reduce mobile, high-valence species into low-toxicity, low-solubility precipitates, thereby facilitating wastewater purification and resource recovery [135–137]. Dai et al. [138] demonstrated that g-$C_3N_4$-based S-scheme heterojunctions enhance interfacial carrier separation and increase the reduction potential of CB electrons toward radionuclides. Mechanistically, a rigorous chemical distinction must be established between true photocatalytic reduction and photo-assisted precipitation during uranium extraction. Under anaerobic conditions in the presence of organic hole scavengers, high-reduction CB electrons can directly reduce soluble hexavalent U(VI) (e.g., $UO_2^{2+}$) to insoluble tetravalent U(IV) precipitates (such as $UO_2$ nanocrystals) [139]. Conversely, in aerated aqueous environments without sacrificial agents, extraction occurs via photo-assisted precipitation: high-energy conduction-band electrons reduce dissolved $O_2$ into $O_2^{\bullet-}$ and subsequent $H_2O_2$, which subsequently complexes with uranyl ions to precipitate solid studtite $(UO_2)O_2 \cdot 2H_2O$ onto the catalyst surface. In this latter pathway, uranium remains strictly in the hexavalent state (+6), representing a reactive crystallization route rather than a valence reduction process. Dai et al. [140] developed an S-scheme $ZnIn_2S_4$/g-$C_3N_4$ heterojunction for U(VI) extraction under ambient air without sacrificial agents. High-reduction electrons in the g-$C_3N_4$ CB activated dissolved $O_2$ to generate $O_2^{\bullet-}$ and $H_2O_2$, while the interfacial electric field maintained efficient charge separation. Surface analyses confirmed the precipitation of soluble U(VI) into insoluble $(UO_2)O_2 \cdot 2H_2O$ on the catalyst surface. The composite retained over 85% U(VI) removal after five consecutive cycles in the presence of competing co-ions. Mechanistically, the proposed S-scheme pathway was rigorously corroborated via contact potential difference measurements (KPFM), confirming a 0.42 V Fermi-level gradient and directional built-in electric field, while transient absorption spectroscopy validated the preferential recombination of non-effective carriers across the staggered interface. Constructing heterojunctions over g-$C_3N_4$ maximally retains high-reduction conduction band electrons ($E_{CB} \approx -1.1$ to $-1.3$ V vs. NHE), supplying formidable thermodynamic overpotentials to convert soluble high-valence ions into insoluble low-valence precipitates. For radionuclide remediation, Liu et al. [141] fabricated a Z-scheme g-$C_3N_4$/$TiO_2$ composite that removed >99% of aqueous U(VI) within 25 min under UV/solar light ($k$ = 0.2222 $min^{-1}$, 56.97 times that of pristine g-$C_3N_4$). U 4f XPS confirmed the formation of U(IV) (doublets at 379.6 and 390.4 eV), and the Z-scheme preserves the strongly reducing g-$C_3N_4$ conduction-band electrons that drive (U(VI) → U(V) → U(IV)). Liu et al. [142] tuned the N-doped state of polymeric carbon nitride (UMCN) to enrich delocalized electrons that activate peroxydisulfate (PDS); with PDS and $H_2O_2$ coexisting, 100% U(VI) photoreduction was achieved within 20 min. The U(VI) removal ratio was essentially retained over five successive cycling runs (Figure 6a),

while U 4f XPS confirmed genuine valence reduction rather than mere adsorption: the U(VI) peaks at 381.710 and 392.623 eV were shifted to 381.290 and 392.131 eV after irradiation, characteristic of U(IV) (Figure 6b). Radical-trapping experiments and theoretical calculations further indicated that PDS-derived sulfate radicals cooperate with photogenerated electrons through coupled radical and electron-transfer pathways (Figure 6c). Ajiboye et al. [143] constructed a ternary $Cu_{3.21}Bi_{4.79}S_9$/g-$C_3N_4$ heterojunction achieving 92.77% visible-light photoreduction of Cr(VI) ($k$ = 0.0393 $min^{-1}$, a 5.17-fold acceleration over the pristine chalcogenide) (Figure 6d). Crucially, surface zeta-potential determinations illuminated why acidic conditions (pH 2) are indispensable: the positively charged catalyst surface (+12.95 mV) electrostatically attracts negatively charged chromate species ($Cr_2O_7^{2-}$/$HCrO_4^-$), dramatically mitigating interfacial mass-transfer resistance. Furthermore, evaluating real water-matrix perturbations revealed vital engineering boundaries: unlike simple sacrificial scavengers (e.g., methanol) that accelerate reduction, coexisting recalcitrant aromatic pollutants (e.g., bisphenol) and competing heavy-metal cations (e.g., $Pb^{2+}$ and $Ag^+$) induced profound antagonistic effects, prolonging the reduction half-life by over ten-fold due to competitive active-site occupancy and parasitic electron consumption (Figure 6e). Radical quenching assays confirmed that free photogenerated electrons ($e^-$) were the primary reductants governing the detoxification process (Figure 6f).

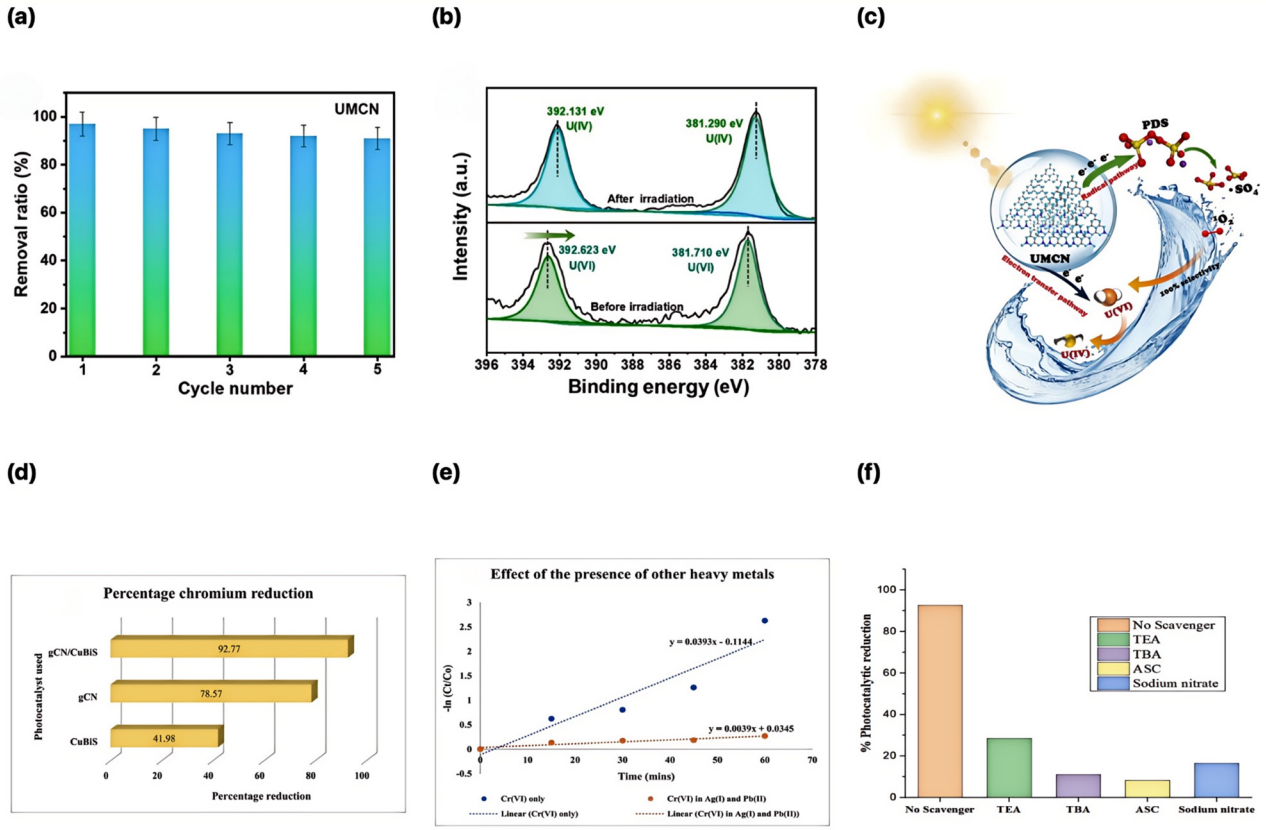



**Figure 6.** Photocatalytic reduction performance and mechanistic analysis of high-valence heavy metal ions over g-$C_3N_4$-based heterojunctions. (**a**) Reusability of UMCN, showing the U(VI) removal ratio over five successive cycling runs; (**b**) high-resolution U 4f XPS spectra recorded before and after irradiation, in which the U(VI) peaks at 381.710 and 392.623 eV shift to 381.290 and 392.131 eV, characteristic of U(IV); and (**c**) Schematic illustration of the proposed photocatalytic mechanism for selective U(VI) reduction over UMCN in the presence of PDS under light irradiation. The green arrow

labeled "Radical pathway" indicates the transfer of photogenerated electrons to PDS to generate active radical species The black curved arrow labeled "Electron transfer pathway" represents the direct transfer of photogenerated electrons to the adsorbed U(VI) species. The yellow curved arrow with "100% selectivity" denotes the highly selective target attack, and the orange curved arrow signifies the reduction of high-valence soluble U(VI) to low-valence U(IV) precipitate. The blue sphere (left) represents UMCN with its embedded photoexcited electrons, while the top molecular models represent PDS activation products, and the bottom models indicate the U(VI) to U(IV) transformation. Reproduced from Ref. [142] under CC BY 4.0 license; (**d**) photocatalytic Cr(VI) reduction efficiency of pristine Cu3.21Bi4.79S9, pure g-C3N4 and Cu3.21Bi4.79S9/g-C3N4 nanocomposite and (**e**) effect of co-existing Ag(I) and Pb(II) ions on the photoreduction kinetics of Cr(VI); (**f**) radical scavenging results for determining the primary reactive species involved in Cr(VI) reduction. Reproduced from Ref. [143] under CC BY 4.0 license.

Similarly, Yang et al. [144] synthesized flower-like $Bi_2S_3$/g-$C_3N_4$ composites via a polyethylene glycol (PEG)-assisted route, reducing soluble Cr(VI) to less toxic Cr(III) under visible light. Guided by a direct Z-scheme pathway, high-energy electrons in the g-$C_3N_4$ CB ($E_{CB} \approx -1.63$ V vs. NHE, as reported under the measurement conditions of Ref. [144]) crossed the activation overpotential to rapidly reduce Cr(VI) to Cr(III), while photogenerated holes and derived $O_2^{\bullet-}$ drove the concurrent degradation of coexisting organic dyes. In an S-scheme g-$C_3N_4$/$Bi_2WO_6$ system, coexisting organic pollutants acted as hole scavengers to suppress carrier recombination, accelerating Cr(VI) reduction kinetics [145]. Concurrently, high-reduction electrons in the g-$C_3N_4$ CB ($E_{CB} \approx -1.1$ to $-1.63$ V vs. NHE) offer a strong thermodynamic driving force to drive the reduction of Cr(VI) to Cr(III), as the reduction potentials of Cr(VI) couples (such as $HCrO_4^-/Cr^{3+}$ at +1.35 V vs. NHE, and $Cr_2O_7^{2-}/Cr^{3+}$ at +1.33 V vs. NHE at pH 0) are highly positive. Furthermore, the speciation and redox thermodynamics of Cr(VI) are strongly pH-dependent: acidic conditions dramatically favor the reduction kinetics because protons participate directly in the electron-transfer process, shifting the equilibrium toward rapid reduction of $HCrO_4^-$, whereas alkaline conditions favor the less reactive $CrO_4^{2-}$ species [146].

**Table 2.** Representative performance of g-$C_3N_4$-based heterojunctions in photocatalytic water purification (compiled from the studies reviewed in Section 5).

| Heterojunction (Mechanism) | Target Contaminant | Operational Conditions (Dosage, Pollutant Conc., pH, Matrix) | Irradiation Source & Wavelength | Reaction Time (h/min) | Kinetic Rate Constant (*k*) | Mineralization /Removal Efficiency | Cyclic Reusability | Ref. |
|---|---|---|---|---|---|---|---|---|
| $MoO_{3-x}$/g-$C_3N_4$ (Direct Z-scheme) | Polyaniline microplastics (PANI-MPs) | Cat.: 0.40 g/L; PANI: 10 mg/L; pH = 6.8; ultrapure water | 500 W Xe lamp ($\lambda \geq$ 420 nm) | 7 d (168 h) | $k$ = 0.48 $d^{-1}$ | 97% degradation; oligomer fragmentation confirmed by LC-MS | High photostability over prolonged run | [115] |
| g-$C_3N_4$/$WO_3$ (Direct Z-scheme) | Tetracycline hydrochloride (TC-HCl) | Cat.: 1.0 g/L; TC-HCl: 30 mg/L; pH = 4.4; aqueous solution | 300 W Xe lamp ($\lambda >$ 400 nm) | 180 min | $k$ = 0.01420 $min^{-1}$ (17.7× pristine g-$C_3N_4$) | 93.3% degradation; dual ROS ($O_2^{\bullet-}$ and ·OH) verified by ESR | 4 cycles (97.8% retention) | [116] |
| g-$C_3N_4$/$Cr_2O_3$ (S-scheme) | Tetracycline (TC) | Cat.: 0.20 g/L; TC: 10 mg/L; natural surface water/river water | 300 W Xe lamp ($\lambda \geq$ 420 nm) | 50 min | $k$ = 0.03121 $min^{-1}$ (5.71× pristine g-$C_3N_4$) | 83.4% TC degradation; 63.8% TOC mineralization; phytotoxicity eliminated | 5 cycles (high stability) | [119] |

**Table 2.** *Cont.*

| Heterojunction (Mechanism) | Target Contaminant | Operational Conditions (Dosage, Pollutant Conc., pH, Matrix) | Irradiation Source & Wavelength | Reaction Time (h/min) | Kinetic Rate Constant (*k*) | Mineralization /Removal Efficiency | Cyclic Reusability | Ref. |
|---|---|---|---|---|---|---|---|---|
| ZnO@CA-modified g-$C_3N_4$ (S-scheme) | Perfluorooctanoic acid (PFOA) | Cat.: 0.53 g/L; PFOA: 53 mg/L; optional PMS (0.53 g/L) | 300 W Xe lamp | 120 min | $k$ = 0.468 $h^{-1}$ (0.868 $h^{-1}$ with PMS) | ~59% degradation (~79% with PMS); stepwise defluorination into $F^-$ & $CO_2$ | 4 cycles (robust durability) | [120] |
| g-$C_3N_4$/BiOBr (S-scheme) | Methylene blue; Congo red; tetracycline | Cat.: 0.50 g/L; MB: 20 mg/L; CR: 20 mg/L; TC: 50 mg/L river water (pH 4–10) | 300 W Xe lamp (λ > 420 nm) | 90 min | $k$(MB) = 0.02689 $min^{-1}$ | 90.8% MB; 99.2% CR; 89% TC | 5 cycles (>80.2% retention) | [122] |
| g-$C_3N_4$/$Bi_2O_2CO_3$ (Direct Z-scheme) | Tetracycline hydrochloride (TC-HCl) | Cat.: 1.0 g/L; TC-HCl: 44.4 mg/L ($1 \times 10^{-4}$ M); neutral pH | Simulated solar light (Xe lamp) | 60 min | $k$ = 0.0608 $min^{-1}$ (5.1× porous g-$C_3N_4$)) | 97.4% degradation within 60 min | 5 cycles (no distinct loss) | [124] |
| $Co_3O_4$/g-$C_3N_4$ (p-n/Type-II) | Rhodamine B (RhB) | Cat.: 0.20 g/L; RhB: 10 mg/L; aqueous matrix | Simulated solar light (300 W Xe lamp) | 40 min | $k$ = 0.0703 $min^{-1}$ (2.93× pristine g-$C_3N_4$) | 97.6% degradation; $O_2^{\bullet-}$ and $h^+$ dominant | 3 cycles (no significant loss) | [127] |
| AgBr/g-$C_3N_4$ (Direct Z-scheme) | *Escherichia coli* (*E. coli*) | Cat.: 0.10 g/L; $10^7$ CFU/mL; pH = 7.0; saline solution (0.85% NaCl) | 300 W Xe lamp (λ > 420 nm) | 90 min | $k$ = 0.078 $min^{-1}$ | 100% disinfection (complete cellenvelope destruction & cytoplasmic leakage) | 4 cycles (>99.9% bactericidal rate) | [129] |
| UCN/RGO/SCN (Homojunction) | *E. coli* & *S. aureus* | Cat.: 1.0 g/L; $10^7$ CFU/mL; saline solution | 300 W Xe lamp (λ > 400 nm) | 180 min | $k \approx$ 0.0392 $min^{-1}$ | 99.92% (*E. coli*); 99.85% (*S. aureus*) | 5 cycles (sustained activity) | [130] |
| $ZnIn_2S_4$/g-$C_3N_4$ (S-scheme) | Uranium extraction (U(VI)) | Cat.: 0.20 g/L; U(VI): 50 mg/L; pH = 5.0; air atmosphere; natural water | 300 W Xe lamp (λ > 420 nm) | 480 min | $k$ = 0.015 $min^{-1}$ | >94% removal via reactive surface precipitation as $(UO_2)O_2 \cdot 2H_2O$ | 5 cycles (>85% extraction retained) | [140] |
| $Bi_2S_3$/g-$C_3N_4$ (Direct Z-scheme) | Cr(VI) & Rhodamine B (RhB) | Cat.: 0.50 g/L; Cr(VI): 20 mg/L, RhB: 10 mg/L; pH = 2.0; acidic wastewater | 300 W Xe lamp (λ > 420 nm) | 30 min | $k$ = 0.228 $min^{-1}$ (Cr(VI) reduction) | 100% Cr(VI) reduction to Cr(III); simultaneous 96% RhB decolorization | 4 cycles (>90% reduction efficiency retained) | [144] |

To synthesize the interfacial physics, reactive species generation, and technological trade-offs discussed across preceding sections, Figure 7 illustrates a holistic conceptual framework connecting heterojunction configurations (Type-I, Type-II, direct Z-scheme, and S-scheme) to their respective carrier transfer trajectories, preserved redox-active sites, dominant reactive oxygen species (ROS) and representative water remediation targets. This holistic author-generated synthesis provides an actionable decision-making matrix for tailoring g-$C_3N_4$-based architectures toward specific environmental decontamination challenges.

| Evaluation Dimension | Type-I Heterojunction | Type-II Heterojunction | Direct Z-Scheme | S-Scheme Junction |
|---|---|---|---|---|
| 1. Interfacial Transfer & Band Alignment | • Straddling band alignment<br>• Bidirectional charge accumulation onto single narrow-bandgap host | • Staggered band offset<br>• Classical bidirectional separation: $e^-$ to lower CB, $h^+$ to higher VB | • Staggered band offset<br>• Interfacial recombination of inactive $e^-$(SC-I) and $h^+$(SC-II) | • Band bending + IEF steering<br>• Coulombic attraction guides selective interfacial annihilation |
| 2. Preserved Redox Sites | • Low-potential CB (weak reduction)<br>• Low-potential VB (weak oxidation) | • Moderate CB reduction site<br>• Moderate VB oxidation site | • High-reduction CB of SC-II<br>• Deep-oxidation VB of SC-I | • Highest reduction CB on RP<br>• Deepest oxidation VB on OP |
| 3. Dominant ROS | • **Poor ROS generation**<br>• Trace $^1O_2$, negligible •OH | • **Modest $O_2$•$^-$ generation**<br>• Sub-optimal •OH production | • **Vigorous $O_2$•$^-$ and •OH**<br>• Robust hydroxyl radical pathways | • **Maximum dual-ROS flux**<br>• High-yield $O_2$•$^-$, •OH, and $h^+$ |
| 4. Target Water Applications | • **Sensitized dye fading**<br>• Simple photothermal sterilization<br>• Highly ineffective for recalcitrant pollutant destruction | • **Azo dye discoloration**<br>• Partial degradation of simple phenols<br>• Non-selective disinfection | • **Recalcitrant antibiotic removal**<br>• Persistent Organic Pollutants (POPs)<br>• Enhanced mineralization rates | • **Synchronous Cr(VI) reduction & antibiotic mineralization**<br>• Microplastic depolymerization<br>• High-salinity real wastewater |

**Figure 7.** Schematic summary correlating heterojunction classifications (Type-I, Type-II, direct Z-scheme, and S-scheme) with their interfacial charge-transfer dynamics, preserved redox reaction centers, dominant reactive oxygen species (ROS), targeted aquatic decontamination domains, and respective limitations.

## 6. Conclusions and Perspectives

This review systematically summarized the structural features, synthetic methods, and environmental applications of g-$C_3N_4$-based heterojunctions in photocatalytic water purification. While g-$C_3N_4$ exhibits favorable band positions, non-toxicity, and stability, pristine formulations are hindered by rapid carrier recombination, narrow optical absorption, and low active-site exposure. Heterojunction construction, particularly Z-scheme and S-scheme configurations, spatially separates electron–hole pairs while preserving strong redox driving forces, establishing effective platforms for emerging pollutant degradation, microbial disinfection, and toxic metal reduction.

To translate laboratory-scale g-$C_3N_4$ heterojunction photocatalysis into engineering practice, future research must address five key dimensions:

(1) Real-World Water Matrix Resilience and Selective Interfacial Catalysis: The vast majority of reported studies evaluate degradation kinetics in deionized water, masking critical matrix effects encountered in municipal and industrial effluents. Future work must routinely benchmark photocatalysts against ubiquitous natural organic matter (NOM, e.g., humic and fulvic acids) that block active sites and light penetration, as well as background inorganic anions ($HCO_3^-$, $Cl^-$, $SO_4^{2-}$ and $NO_3^-$) that act as radical scavengers. Engineering surface hydrophilicity/charge repulsion and creating molecularly imprinted or size-selective catalytic interfaces are vital strategies to resist fouling and preserve selective contaminant destruction.

(2) Macroscopic Shaping, Catalyst Immobilization, and Continuous Membrane Reactors: Post-treatment separation and recovery of sub-micron suspension powders impose prohibitive energy and capital costs. Research should shift aggressively from loose powder systems to macroscopically engineered architectures. Promising directions include: (i) 3D monolithic shaping via direct ink writing or additive manufacturing; (ii) durable immobilization onto flow-through porous substrates (e.g., polyurethane sponges, ceramic foams, stainless-steel meshes, and optical-fiber arrays); and (iii) integration into continuous photocatalytic membrane reactors (PMRs) with submerged or self-cleaning filtration modules to prevent catalyst loss.

(3) AI-assisted Rational Design: Empirical trial-and-error synthesis of heterojunction interfaces must be replaced by data-driven predictive paradigms. Future research should combine first-principles hybrid-functional DFT calculations (evaluating interfacial binding energy, planar work functions, and charge density redistribution) with machine learning (ML) algorithms. Constructing standardized, high-quality feature libraries of component band alignments, surface termination states, and interfacial charge injection kinetics will enable accelerated screening of stable, highly active heterojunction candidate pairs prior to laboratory synthesis.

(4) Multi-Physics CFD Modeling and Full-Scale Photoreactor Design: Laboratory assessments using small batch beakers under perpendicular top-irradiation fail to represent fluid-mechanical and optical realities. Future engineering efforts must utilize computational fluid dynamics (CFD) coupled with radiative transfer models (RTM) to simulate local volumetric light absorption, turbulent fluid mixing, and substrate mass-transfer boundary layers. Developing continuous-flow, scalable solar reactor topologies—such as compound parabolic concentrators (CPCs), spinning disc reactors, and tubular thin-film flow configurations—is critical to maximizing photonic efficiency per unit footprint.

(5) Comprehensive Toxicological Profiling and Life-Cycle Assessment (LCA): Complete pollutant disappearance (decolorization) frequently generates persistent or more toxic transformation intermediates (e.g., hydroxylated or chlorinated derivatives). Subsequent evaluations must rigorously quantify total organic carbon (TOC) mineralization and couple high-resolution mass spectrometry (LC-QTOF-MS/MS) with in vivo and in vitro ecotoxicity screenings (e.g., Vibrio fischeri microtoxicity and zebrafish embryo assays). Concurrently, cradle-to-grave life-cycle assessments (LCA) and techno-economic analyses (TEA) must be standardized, reporting electrical energy per order ($E_{EO}$) and carbon emissions to prove tangible advantages over conventional advanced oxidation processes (AOPs).

**Author Contributions:** Conceptualization, J.Z. and H.C.; methodology, C.L.; validation, H.Z.; formal analysis, S.D.; investigation, S.D., Z.L., H.L., H.J., Y.L., C.L., H.Z. and S.G.; data curation, J.Z., Z.L. and H.J.; writing—original draft preparation, J.Z.; writ-ing—review and editing, H.C. and D.L.; visualization, H.L., Y.L. and S.G.; supervision, H.C.; funding acquisition, H.C. and D.L. All authors have read and agreed to the published version of the manuscript.

**Funding:** This work was supported by the Guangdong Provincial Program for Young Innovative Talents in General Higher Education Institutions (Grant No. 2024KQNCX169), and the Testing Fund Project of the Analytical and Testing Center of Foshan University.

**Data Availability Statement:** No new data were created or analyzed in this study. Data sharing is not applicable to this article.

**Acknowledgments:** During the preparation of this manuscript, the authors used Gemini 3.8Flash solely for the purpose of English language polishing (polishing punctuation and improving sentence flow). The authors have reviewed and edited the output and take full responsibility for the content of this publication.

**Conflicts of Interest:** The authors declare no conflicts of interest.

## References

1. Balakrishnan, A.; Chinthala, M.; Kumar, A.; Dayanandan, N.; Trivedi, S. Recent advances on graphitic carbon nitride-based homojunction as effective photocatalysts for energy and environmental remediation. *Int. J. Hydrogen Energy* **2025**, *98*, 1020–1033. [CrossRef]
2. Rout, P.R.; Zhang, T.C.; Bhunia, P.; Surampalli, R.Y. Treatment technologies for emerging contaminants in wastewater treatment plants: A review. *Sci. Total Environ.* **2021**, *753*, 141990. [CrossRef] [PubMed]

3. Patel, M.; Kumar, R.; Kishor, K.; Mlsna, T.; Pittman, C.U.; Mohan, D. Pharmaceuticals of emerging concern in aquatic systems: Chemistry, occurrence, and advanced treatment methods. *Chem. Rev.* **2019**, *119*, 3510–3673. [CrossRef] [PubMed]
4. Ong, W.J.; Tan, L.L.; Ng, Y.H.; Yong, S.T.; Chai, S.P. Graphitic Carbon Nitride ($g\text{-}C_3N_4$)-Based Photocatalysts for Artificial Photosynthesis and Environmental Remediation: Are We a Step Closer to Achieving Sustainability? *Chem. Rev.* **2016**, *116*, 7159–7329. [CrossRef] [PubMed]
5. Ajmal, Z.; Qadeer, A.; Hayat, A.; Fadhali, M.M.; Khan, M.A.; Mahmood, A.; Ibrahim, E.H.; Imran, M.; Rehman, M.S.U.; Bashir, S.; et al. Carbon-nitride based novel materials for energy conversion and storage: Recent advances, current challenges, prospects and environmental consequences. *J. Mater. Sci. Technol.* **2026**, *257*, 185–221. [CrossRef]
6. Yang, S.; Gong, Y.; Zhang, J.; Zhan, L.; Ma, L.; Fang, Z.; Vajtai, R.; Wang, X.; Ajayan, P.M. Exfoliated graphitic carbon nitride nanosheets as efficient catalysts for hydrogen evolution under visible light. *Adv. Mater.* **2013**, *25*, 2452–2456. [CrossRef] [PubMed]
7. Zheng, Y.; Lin, L.; Wang, B.; Wang, X. Graphitic carbon nitride polymers toward sustainable photoredox catalysis. *Angew. Chem. Int. Ed.* **2015**, *54*, 12868–12884. [CrossRef] [PubMed]
8. Wang, X.; Maeda, K.; Thomas, A.; Takanabe, K.; Xin, G.; Carlsson, J.M.; Domen, K.; Antonietti, M. A metal-free polymeric photocatalyst for hydrogen production from water. *Nat. Mater.* **2009**, *8*, 76–80. [CrossRef] [PubMed]
9. Zheng, Y.; Liu, J.; Liang, J.; Jaroniec, M.; Qiao, S.Z. Graphitic carbon nitride materials: Controllable synthesis and applications in fuel cells and photocatalysis. *Energy Environ. Sci.* **2012**, *5*, 6717–6731. [CrossRef]
10. Zou, S.; An, Z.; Tang, Y.; Xiong, B.; Wang, L.; Shi, W.; Li, C.; Guo, F. Construction of industrial waste red-mud/graphitic carbon nitride S-scheme heterojunction for efficient photocatalytic $H_2$ production. *J. Alloys Compd.* **2025**, *1037*, 182448. [CrossRef]
11. Gu, Y.; Li, Y.; Feng, H.; Han, Y.; Li, Z. Built-in Electric Field Induced S-Scheme $g\text{-}C_3N_4$ Homojunction for Efficient Photocatalytic Hydrogen Evolution: Interfacial Engineering and Morphology Control. *Nano Res.* **2024**, *17*, 4961–4970. [CrossRef]
12. Veiga-del-Baño, J.M.; Pérez-Lucas, G.; Andreo-Martínez, P.; Navarro, S. Bibliometric analysis on graphitic carbon nitride ($g\text{-}C_3N_4$) as photocatalyst for the remediation of water polluted with contaminants of emerging concern. *Catalysts* **2025**, *15*, 115. [CrossRef]
13. Xu, Q.; Zhang, L.; Yu, J.; Wageh, S.; Al-Ghamdi, A.A.; Jaroniec, M. Direct Z-Scheme Photocatalysts: Principles, Synthesis, and Applications. *Mater. Today* **2018**, *21*, 1042–1063. [CrossRef]
14. Wen, J.; Xie, J.; Chen, X.; Li, X. A review on $g\text{-}C_3N_4$-based photocatalysts. *Appl. Surf. Sci.* **2017**, *391*, 72–123. [CrossRef]
15. Liang, C.; Niu, H.Y.; Guo, H.; Niu, C.G.; Yang, Y.Y.; Liu, H.Y.; Tang, W.W.; Feng, H.P. Efficient photocatalytic nitrogen fixation to ammonia over bismuth monoxide quantum dots-modified defective ultrathin graphitic carbon nitride. *Chem. Eng. J.* **2021**, *406*, 126868. [CrossRef]
16. Huang, B.; Xu, K.; Zhao, Y.; Li, B.; Jiang, S.; Liu, Y.; Huang, S.; Yang, Q.; Gao, T.; Xie, S.; et al. Review of the versatility and application potentials of $g\text{-}C_3N_4$-based S-scheme heterojunctions in photocatalytic antibiotic degradation. *Molecules* **2025**, *30*, 1240. [CrossRef] [PubMed]
17. Zheng, M.; Li, Y.; Ma, F.; Liang, M.; Zhang, X.; Wang, J.; Zhao, J.; Li, W.; Shao, Y.; Wu, X. Mesoporous graphitic carbon nitride nanostructure-based antibiotic degradation via synergistic adsorption and photocatalysis: A review. *ACS Appl. Nano Mater.* **2026**, *9*, 4053–4080. [CrossRef]
18. Lu, X.; Zhu, M.; Chen, D.; Wu, J.; Gao, S.; Zhao, Y.; Yang, J.; Li, S.; Meng, J. Preparation, modification, and application of graphitic carbon nitride in photocatalytic degradation of antibiotics. *Processes* **2025**, *13*, 3365. [CrossRef]
19. Tul Ain, T.; Raza, M.A.; Javaid, A.; Imran, M.; Latif, S.; Mitu, L.; Ciolan, F. Bismuth-Based Magnetic Z-Scheme Heterojunctions as Emerging Photocatalysts for the Environmental Remediation of Pharmaceuticals. *Arab. J. Chem.* **2025**, *18*, 532025. [CrossRef]
20. Zhao, Z.; Yuan, X.; Pei, S.; Zhang, S. Graphitic carbon nitride-based photocatalysts for uranium reduction and extraction: From fundamentals to applications. *Catalysts* **2026**, *16*, 249. [CrossRef]
21. Li, C.; Harikrishnan, L.; Ding, L.; Pitcheri, R.; Qi, K. Graphitic carbon nitride-based photocatalysts and sonocatalysts for energy and environment. *Renew. Sustain. Energy Rev.* **2026**, *226*, 116435. [CrossRef]
22. Chaluvachar, P.; Sudhakar, Y.; Mahesha, G.; Nair, V.G.; Desai, N.; Pai, D.K. Emerging role of graphitic carbon nitride in advanced supercapacitors: A comprehensive review. *J. Energy Chem.* **2025**, *103*, 498–524. [CrossRef]
23. Song, J.; Dai, X.; He, M.; Song, Y.; Yang, J. A review of recent advances in carbon nitride photocatalysts for $CO_2$ reduction. *Coord. Chem. Rev.* **2026**, *554*, 217613. [CrossRef]
24. Heyd, J.; Scuseria, G.E.; Ernzerhof, M. Hybrid functionals based on a screened Coulomb potential. *J. Chem. Phys.* **2003**, *118*, 8207–8215. [CrossRef]
25. Toroker, M.C.; Kanan, D.K.; Alidoust, N.; Isseroff, L.Y.; Liao, P.; Carter, E.A. First principles scheme to evaluate band edge positions in potential transition metal oxide photocatalysts and photoelectrodes. *Phys. Chem. Chem. Phys.* **2011**, *13*, 16644–16654. [CrossRef] [PubMed]
26. Zhang, J.; Chen, Y.; Wang, X. Two-dimensional covalent carbon nitride nanosheets: Synthesis, functionalization, and applications. *Energy Environ. Sci.* **2015**, *8*, 3092–3108. [CrossRef]

27. Taghipour, S.; Hussain Solangi, N.; Anjum, A.; Hussin, F.; Ali Mazari, S.; Mujawar Mubarak, N.; Ataie-Ashtiani, B.; Lee, U.; Kheireddine Aroua, M.; Moon, J.H. Catalytic conversion of $CO_2$ using carbon nitride-based catalysts: Recent advances, opportunities, and challenges. *Coord. Chem. Rev.* **2024**, *511*, 215831. [CrossRef]
28. Budiarso, I.J.; Dabur, V.A.; Rachmantyo, R.; Judawisastra, H.; Hu, C.; Wibowo, A. Carbon nitride-and graphene-based materials for the photocatalytic degradation of emerging water pollutants. *Mater. Adv.* **2024**, *5*, 2668–2688. [CrossRef]
29. Wu, L.; Yang, D.; Dong, Y.; Wang, Z.; Zhang, Y.; Wang, T.; Cheng, L.; Wang, Y.; Wu, Y. Enhanced $CO_2$ reduction via S-scheme heterojunction of amorphous/crystalline metal-free carbon nitride photocatalysts. *Chem. Eng. J.* **2024**, *500*, 156777. [CrossRef]
30. Ahmed, M.A.; Mahmoud, S.A.; Mohamed, A.A. Unveiling the photocatalytic potential of graphitic carbon nitride (g-$C_3N_4$): A state-of-the-art review. *RSC Adv.* **2024**, *14*, 25629–25662. [CrossRef] [PubMed]
31. Sahoo, S.K.; Acharya, L.; Biswal, L.; Priyadarshini, P.; Parida, K. Recent advancements in graphitic carbon nitride based direct Z- and S-scheme heterostructures for photocatalytic $H_2O_2$ production. *Inorg. Chem. Front.* **2024**, *11*, 4914–4973. [CrossRef]
32. Wang, Z.; Wei, Y.; Liu, C.; Teng, Y.; Shu, P.; Peng, X. Rare earth doping-regulated g-$C_3N_4$-based photocatalysts: Heterojunction construction, mechanisms, and synergistic applications in energy and environment. *Adv. Sustain. Syst.* **2026**, *10*, 70458. [CrossRef]
33. Lin, J.; Lu, X.; Zhang, L.; Gao, F. 1D metal nitrides-based heterojunctions as efficient photoanodes for photoelectrochemical water splitting. *Int. J. Hydrogen Energy* **2024**, *71*, 903–915. [CrossRef]
34. Yan, Y.; Meng, Q.; Tian, L.; Cai, Y.; Zhang, Y.; Chen, Y. Engineering of g-$C_3N_4$ for Photocatalytic Hydrogen Production: A Review. *Int. J. Mol. Sci.* **2024**, *25*, 8842. [CrossRef] [PubMed]
35. Pérez-Torres, A.F.; Hernández-Barreto, D.F.; Bernal, V.; Giraldo, L.; Moreno-Piraján, J.C.; da Silva, E.A.; Alves, M.D.C.M.; Morais, J.; Hernandez, Y.; Cortés, M.T.; et al. Sulfur-doped g-$C_3N_4$ heterojunctions for efficient visible light degradation of methylene blue. *ACS Omega* **2023**, *8*, 47821–47834. [CrossRef] [PubMed]
36. Zhao, Y.; Zhang, H.T.; Zhang, W.M.; Wen, H.Z.; Wan, X.Y.; Xie, Y.L.; Pan, L. Molten-salt-engineered graphitic $C_3N_4/ZnIn_2S_4$ composites for accelerated charge separation in photocatalytic hydrogen production. *ACS Appl. Nano Mater.* **2025**, *8*, 19619–19629. [CrossRef]
37. Low, J.; Yu, J.; Jaroniec, M.; Wageh, S.; Al-Ghamdi, A.A. Heterojunction photocatalysts. *Adv. Mater.* **2017**, *29*, 1601694. [CrossRef] [PubMed]
38. Eroglu, Z.; Turbedaroglu, O.; Kubanaliev, T.; Alemdar, S.; Kilic, H.; Metin, O. Few layer phosphorene/reduced graphene oxide/graphitic carbon nitride ternary heterojunctions for sustainable photoredox C-H functionalization of heteroarenes. *Inorg. Chem. Front.* **2026**, *13*, 6189–6202. [CrossRef]
39. Wang, C.; Zheng, H.; Ma, R.; Zheng, X.; Guan, X. $Ag_2S/Zn^{2+}$-decorated g-$C_3N_4$ type-II heterojunction with wide-spectrum response: Construction and photocatalytic performance in ciprofloxacin degradation. *Molecules* **2025**, *30*, 1417. [CrossRef] [PubMed]
40. Li, Y.; Shu, S.; Huang, L.; Liu, J.; Liu, J.; Yao, J.; Liu, S.; Zhu, M.; Huang, L. Construction of a novel double S-scheme structure $WO_3$/g-$C_3N_4$/BiOI: Enhanced photocatalytic performance for antibacterial activity. *J. Colloid Interface Sci.* **2023**, *633*, 60–71. [CrossRef] [PubMed]
41. Marschall, R. Semiconductor Composites: Strategies for Enhancing Charge Carrier Separation to Improve Photocatalytic Activity. *Adv. Funct. Mater.* **2014**, *24*, 2421–2440. [CrossRef]
42. Cheng, S.; Fang, Y.; Yang, S.; Gao, Q.; Cai, X.; Zhang, S. Synergistic dual-cocatalyst modified $TiO_2$/g-$C_3N_4$ heterojunctions for efficient photocatalytic overall water splitting. *Chem. Res. Chin. Univ.* **2025**, *41*, 751–759. [CrossRef]
43. Liu, Y.; Sun, G.; Cao, Y.; Li, X.; Li, Z.; Chen, Z. Synergistic elimination of antibiotic resistance genes and tetracycline antibiotics in wastewater via a Z-scheme $Bi_2WO_6$/g-$C_3N_4$ heterojunction. *RSC Adv.* **2026**, *16*, 16424–16441. [CrossRef] [PubMed]
44. Zhang, X.; Gao, X.; Zhao, B.; Wu, N. Enhanced mechanism of a $TiO_2$/g-$C_3N_4$ photoanode in photoelectrocatalytic synergistic persulfate activation for antibiotic degradation. *RSC Adv.* **2025**, *15*, 48969–48977. [CrossRef] [PubMed]
45. Han, P.D.; Dong, G.H.; Zhang, X.J.; Chai, D.F.; Su, T.; Zhang, Z.F.; Zhao, M.; Li, J.L.; Zhang, W.Z. Microwave-assisted preparation of Z scheme heterojunction by anchoring $ZnFe_2O_4$ on tubular-like g-$C_3N_4$ for peroxymonosulfate activation towards levofloxacin degradation. *J. Cent. South Univ.* **2025**, *32*, 894–918. [CrossRef]
46. Ren, Y.; Zeng, D.; Ong, W.J. Interfacial engineering of graphitic carbon nitride (g-$C_3N_4$)-based metal sulfide heterojunction photocatalysts for energy conversion: A review. *Chin. J. Catal.* **2019**, *40*, 289–319. [CrossRef]
47. Sharma, S.K.; Kumar, A.; Anand, B.; Thakur, A.; Saima; Lai, C.W. Heterojunction photocatalysts for improvements and innovation in toluene photo-oxidation under visible light: Recent advances. *J. Alloys Compd.* **2026**, *1056*, 186484. [CrossRef]
48. Meng, Z.; Chen, S.; Yang, P.; Yan, Y.; Jiang, G.; Zhang, Q.; Li, Y. g-$C_3N_4$-based S-scheme heterojunction photocatalyst and its application. *Chin. J. Struct. Chem.* **2026**, *45*, 100889. [CrossRef]
49. Low, J.; Cheng, B.; Yu, J. Surface modification and enhanced photocatalytic $CO_2$ reduction performance of $TiO_2$: A review. *Appl. Surf. Sci.* **2017**, *392*, 658–686. [CrossRef]
50. Sun, W.; Zhu, J.; Zheng, Y. Graphitic carbon nitride heterojunction photocatalysts for solar hydrogen production. *Int. J. Hydrogen Energy* **2021**, *46*, 37242–37267. [CrossRef]

51. Shabbir, A.; Sardar, S.; Mumtaz, A. Mechanistic investigations of emerging type-II, Z-scheme and S-scheme heterojunctions for photocatalytic applications—A review. *J. Alloys Compd.* **2024**, *1003*, 175683. [CrossRef]
52. Chowdhury, A.P.; Anantharaju, K.S.; Keshavamurthy, K.; Swain, S.; Uma, B. A mini-review on Z and S scheme heterojunction bismuth based photocatalysts towards $H_2$ production, $CO_2$ reduction, and pollutant degradation. *Next Mater.* **2025**, *8*, 100918. [CrossRef]
53. Fu, J.; Xu, Q.; Low, J.; Jiang, C.; Yu, J. Ultrathin 2D/2D $WO_3$/g-$C_3N_4$ step-scheme $H_2$-production photocatalyst. *Appl. Catal. B Environ.* **2019**, *243*, 556–565. [CrossRef]
54. Ali, M.; Inam, A.; Alshehri, S.M.; Bando, Y.; Ahamad, T. Interface engineering of COF/semiconductor S-scheme heterojunctions photocatalyst for coupled energy conversion and environmental detoxification. *Int. J. Hydrogen Energy* **2026**, *228*, 154536. [CrossRef]
55. Chen, H.; Huang, L.; Li, X.; Du, J.; Wang, Z.; Chen, L.; Zheng, P.; Nie, C.; Yin, M.; Zhu, W.; et al. Interfacial engineering strategies in bio-heterojunctions for antibacterial therapeutics and biomedical applications. *Acta Biomater.* **2026**, *209*, 120–147. [CrossRef] [PubMed]
56. Yang, C.; Rong, Q.; Shi, F.; Cao, M.; Li, G.; Xin, Y.; Zhang, W.; Zhang, G. Rationally designed S-scheme heterojunction of BiOCl/g-$C_3N_4$ for photodegradation of sulfamerazine: Mechanism insights, degradation pathways and DFT calculation. *Chin. Chem. Lett.* **2024**, *35*, 109767. [CrossRef]
57. Wei, M.; Ou, X.; Wang, Y.; Zhang, M.; Teng, F.; Wang, K. S-scheme heterojunction g-$C_3N_4$/$Bi_2WO_6$ highly efficient degradation of levofloxacin. *Acta Phys.-Chim. Sin.* **2025**, *41*, 100105. [CrossRef]
58. Barik, M.R.; Kumar, J.; Badamali, S.K. Nyctanthes arbor-tristis L. mediated sustainable synthesis of α-$Fe_2O_3$/g-$C_3N_4$ S-scheme heterojunctions for enhanced photocatalytic degradation of tetracycline hydrochloride. *RSC Sustain.* **2025**, *3*, 3582–3600. [CrossRef]
59. Ren, H.; Labidi, A.; Sial, A.; Gao, T.; Xu, X.; Liang, J.; Kang, H.; Liao, Y.; Zhao, K.; Padervand, M.; et al. Carbon quantum dots modified Z and S-scheme heterojunctions for pharmaceutical contaminants photodegradation: State-of-the-art, benefits, and limitations. *Sep. Purif. Technol.* **2024**, *346*, 127508. [CrossRef]
60. Sheraz, M.; Liotta, L.F.; Akram, M.; Wang, R. Next-generation Z-scheme and S-scheme heterojunction photocatalysts for microplastics mineralization. *Coord. Chem. Rev.* **2026**, *557*, 217735. [CrossRef]
61. Lin, J.; Tian, W.; Zhang, H.; Duan, X.; Sun, H.; Wang, H.; Fang, Y.; Huang, Y.; Wang, S. Carbon nitride-based Z-scheme heterojunctions for solar-driven advanced oxidation processes. *J. Hazard. Mater.* **2022**, *434*, 128866. [CrossRef] [PubMed]
62. Helander, M.G.; Greiner, M.T.; Wang, Z.B.; Lu, Z.H. Pitfalls in measuring work function using photoelectron spectroscopy. *Appl. Surf. Sci.* **2010**, *256*, 2602–2605. [CrossRef]
63. Li, L.; Salvador, P.A.; Rohrer, G.S. Photocatalysts with internal electric fields. *Nanoscale* **2014**, *6*, 24–42. [CrossRef] [PubMed]
64. Wang, L.; Cheng, B.; Zhang, L.; Yu, J. In situ irradiated XPS investigation on S-scheme $TiO_2$@$ZnIn_2S_4$ photocatalyst for efficient photocatalytic $CO_2$ reduction. *Small* **2021**, *17*, 2103447. [CrossRef] [PubMed]
65. Li, N.; Ma, Y.; Sun, W. Exploring the Dynamics of Charge Transfer in Photocatalysis: Applications of Femtosecond Transient Absorption Spectroscopy. *Molecules* **2024**, *29*, 3995. [CrossRef] [PubMed]
66. Nosaka, Y.; Nosaka, A.Y. Generation and detection of reactive oxygen species in photocatalysis. *Chem. Rev.* **2017**, *117*, 11302–11336. [CrossRef] [PubMed]
67. Soni, V.; Tarannum, T.; Singh, P.; Van Le, Q.; Nguyen, V.H.; Khan, A.A.P.; Hussain, C.M.; Raizada, P. Advances in photoactive g-$C_3N_5$ derived Z-and S-scheme heterojunctions for energy and environmental catalysis. *J. Environ. Chem. Eng.* **2025**, *13*, 120465. [CrossRef]
68. Zhao, L.; Dai, R.; Tang, Y.; Cheng, X.; Zhou, J.; Shi, B. Constructing a Z-scheme heterojunction on leather waste-derived biochar supporting graphitic carbon nitride for highly-efficient photocatalysis toward water decontamination. *Chem. Eng. J.* **2026**, *535*, 175440. [CrossRef]
69. Ding, X.; Wang, Q.; Liu, H.; Wang, J.; Yan, P.; Chen, H.; Sun, P.; Zhu, X.; Mo, Z.; Xu, H. Research progress of graphitic carbon nitride in photocatalytic hydrogen evolution. *Int. J. Hydrogen Energy* **2025**, *187*, 152004. [CrossRef]
70. Chubenko, E.B.; Maximov, S.E.; Bui, C.D.; Pham, V.T.; Borisenko, V.E. Rapid chemical vapor deposition of graphitic carbon nitride films. *Materialia* **2023**, *28*, 101724. [CrossRef]
71. Du, J.; Ahmad, I.; Ashraf, I.; Ahmed, F.B.; Aslam, A.; Ali, I.; Mohammad, A.; Khasawneh, M.A. Advancements in dual S-scheme heterojunction systems for photocatalytic applications: A mini-review. *Int. J. Hydrogen Energy* **2025**, *100*, 1361–1384. [CrossRef]
72. Ruiz-Santoyo, V.; Cabrera-Germán, D.; Garcia-Carvajal, S.; Arenas-Arrocena, M.C. In Situ Hydrothermal Synthesis of a g-$C_3N_4$—$Bi_2O_3$ Heterojunction for Efficient Photocatalytic Degradation of Tetracycline Hydrochloride. *Top. Catal.* **2026**, *69*, 2016–2031. [CrossRef]
73. Liang, Y.; Jiang, Y. Porous graphitic carbon nitride with engineered carbon vacancies for highly efficient visible-light photocatalytic hydrogen evolution. *Mater. Lett.* **2026**, *424*, 141478. [CrossRef]

74. Li, T.; Zhang, M.; Zhou, S.; Zhou, K.; Han, Y.; Tao, R.; Fan, X. Facile preparation of low-cost, environment-friendly, and high-performance Fe doped g-$C_3N_4$/$Fe_2O_3$ heterojunction photocatalyst for removing gaseous organic pollutant. *J. Alloys Compd.* **2025**, *1010*, 178138. [CrossRef]
75. Sivalingam, A.M. Challenges in utilizing biosynthesized CuO-based photocatalyst heterojunctions for pollutant degradation. *J. Environ. Chem. Eng.* **2026**, *14*, 122597. [CrossRef]
76. Pham, M.T.; Luu, H.Q.; Nguyen, T.M.T.; Tran, H.H.; You, S.J.; Wang, Y.F. Rapid and scalable fabrication of $TiO_2$@g-$C_3N_4$ heterojunction for highly efficient photocatalytic NO removal under visible light. *Aerosol Air Qual. Res.* **2021**, *21*, 210276. [CrossRef]
77. Chen, Z.; Meng, F.; Ren, H.; Zhang, L.; Fu, M.; Zhu, D. One step synthesis of ZnO/g-$C_3N_4$ composite for photocatalytic degradation of methylene blue and emerging contaminants under sunlight. *J. Appl. Polym. Sci.* **2026**, *143*, 70359. [CrossRef]
78. Zhang, G.; Zhang, T.; Li, B.; Jiang, S.; Zhang, X.; Hai, L.; Chen, X.; Wu, W. An ingenious strategy of preparing $TiO_2$/g-$C_3N_4$ heterojunction photocatalyst: In situ growth of $TiO_2$ nanocrystals on g-$C_3N_4$ nanosheets via impregnation-calcination method. *Appl. Surf. Sci.* **2018**, *433*, 963–974. [CrossRef]
79. Imran, M.; Abdullah, A.Z.; Rashid, M.S.; Bakather, O.Y.; Alshoaibi, A.M.; Khan, M.E.; Ali, S.K.; Chaudhary, A.A. Controlled morphology of g-$C_3N_4$/metal oxide-based nanostructures applications in organic pollutant photodegradation: A review. *Inorg. Chem. Commun.* **2026**, *183*, 115681. [CrossRef]
80. Sahu, S.K.; Panda, N.R.; Sahu, D. $MoS_2$-modified g-$C_3N_4$ nanohybrids for the degradation of textile dye in wastewater and microbial disinfection. *J. Indian Chem. Soc.* **2025**, *102*, 102309. [CrossRef]
81. Zhao, W.; Yang, X.; Liu, C.; Qian, X.; Wen, Y.; Yang, Q.; Sun, T.; Chang, W.; Liu, X.; Chen, Z. Facile construction of all-solid-state Z-scheme g-$C_3N_4$/$TiO_2$ thin film for the efficient visible-light degradation of organic pollutant. *Nanomaterials* **2020**, *10*, 600. [CrossRef] [PubMed]
82. Wu, H.; Li, J.; Ma, Y.; Long, Q.; Zhang, P.; Huang, Y.; Zhang, J.; Li, Y.; Yang, C. Exploration of novel g-C3N4/SiO2 aerogel composites for visible-light-driven degradation of methylene blue. *AIP Adv.* **2025**, *15*, 035049. [CrossRef]
83. Gheorghita, S.; Bogatu, C.; Duta, A. $TiO_2$-g-$C_3N_4$ thin film photocatalyst on large substrates for advanced wastewater treatment. *J. Sol-Gel Sci. Technol.* **2023**, *115*, 1065–1078. [CrossRef]
84. Katubi, K.M.; Jabeen, A.; Alrowaili, Z.A.; Al-Buriahi, M.S.; Anwar, M.; Manzoor, A.; Shakir, I.; Warsi, M.F. Sol–gel synthesis of manganese-doped n-type hematite powder photocatalyst supported on g-$C_3N_4$ sheets for the degradation of organic dyes. *J. Sol-Gel Sci. Technol.* **2024**, *111*, 486–499. [CrossRef]
85. Zhang, H.; Liu, F.; Wu, H.; Cao, X.; Sun, J.; Lei, W. In situ synthesis of g-$C_3N_4$/$TiO_2$ heterostructures with enhanced photocatalytic hydrogen evolution under visible light. *RSC Adv.* **2017**, *7*, 40327–40333. [CrossRef]
86. Zhang, P.; Jia, J.; Wang, Y.; Tong, L.; Wang, J.; Li, C.; Dong, H. Metal-free 2D/2D VdW heterojunction fabricated by amorphous covalent triazine frameworks with nitrogen-defect on polymeric carbon nitride towards enhanced photocatalytic performance. *Sep. Purif. Technol.* **2024**, *330*, 125224. [CrossRef]
87. Ong, W.J. 2D/2D Graphitic Carbon Nitride (g-$C_3N_4$) Heterojunction Nanocomposites for Photocatalysis: Why Does Face-to-Face Interface Matter? *Front. Mater.* **2017**, *4*, 11. [CrossRef]
88. Wang, Z.; Zhang, Y.; Yu, Y.; Jia, M.; Tao, X. Promoting photocatalytic degradation of tetracycline over in-situ grown single manganese atoms on polymeric carbon nitride. *Appl. Surf. Sci.* **2022**, *593*, 153458. [CrossRef]
89. Li, H.; Lee, H.Y.; Park, G.S.; Lee, B.J.; Park, J.D.; Shin, C.H.; Hou, W.; Yu, J.S. Conjugated polyene-functionalized graphitic carbon nitride with enhanced photocatalytic water-splitting efficiency. *Carbon* **2018**, *129*, 637–645. [CrossRef]
90. Chen, G.; Zhang, Z.; Liao, Y.; Zhang, Z.; You, Y. Modulating Local Charge Distribution of Carbon Nitride for Promoting Exciton Dissociation and Charge-Induced Reactions. *Small* **2021**, *17*, 2100698. [CrossRef] [PubMed]
91. Li, H.; Zhang, F.; Ma, Y.; Wu, Y.; Sun, S.; Xu, G. In situ construction of η-$Fe_2O_3$/g-$C_3N_4$ Z-scheme heterojunction on nickel foam with efficient interfacial charge transport for enhanced photodegradation of Rhodamine B. *Mater. Sci. Eng. B* **2025**, *312*, 117868. [CrossRef]
92. Kavitha, R.; Nithya, P.; Girish Kumar, S. Noble metal deposited graphitic carbon nitride based heterojunction photocatalysts. *Appl. Surf. Sci.* **2020**, *508*, 145142. [CrossRef]
93. Qi, S.; Liu, X.; Zhang, R.; Zhang, Y.; Xu, H. Preparation and photocatalytic properties of g-$C_3N_4$/BiOCl heterojunction. *Inorg. Chem. Commun.* **2021**, *133*, 108907. [CrossRef]
94. Li, Y.; Rao, F.; Zhong, J.; Li, J. In-situ fabrication of $Bi_2S_3$/g-$C_3N_4$ heterojunctions with boosted $H_2$ production rate under visible light irradiation. *Fuel* **2023**, *341*, 127629. [CrossRef]
95. Wang, W.; Fan, X.; Shu, Z.; Zhou, J.; Meng, D. Sustainable and mild exfoliation of bulk crystalline carbon nitride into ultrathin nanosheets via ion-exchange in pure water. *Carbon* **2023**, *205*, 76–85. [CrossRef]
96. Tuna, Ö. Graphitic carbon nitride quantum dots seeding in $MnTiO_3$ spheres: A novel visible light responsive photocatalyst with high interface charge transfer for antibiotic degradation. *J. Environ. Chem. Eng.* **2024**, *12*, 112593. [CrossRef]

97. Chen, Y.; He, X.; Guo, D.; Cai, Y.; Chen, J.; Zheng, Y.; Gao, B.; Lin, B. Supramolecular electrostatic self-assembly of mesoporous thin-walled graphitic carbon nitride microtubes for highly efficient visible-light photocatalytic activities. *J. Energy Chem.* **2020**, *49*, 214–223. [CrossRef]
98. Li, C.; Kan, C.; Meng, X.; Liu, M.; Shang, Q.; Yang, Y.; Wang, Y.; Cui, X. Self-Assembly 2D $Ti_3C_2$/g-$C_3N_4$ MXene Heterojunction for Highly Efficient Photocatalytic Degradation of Tetracycline in Visible Wavelength Range. *Nanomaterials* **2022**, *12*, 4015. [CrossRef] [PubMed]
99. Wang, H.; Niu, R.; Liu, J.; Guo, S.; Yang, Y.; Liu, Z.; Li, J. Electrostatic self-assembly of 2D/2D $CoWO_4$/g-$C_3N_4$ p–n heterojunction for improved photocatalytic hydrogen evolution: Built-in electric field modulated charge separation and mechanism unveiling. *Nano Res.* **2022**, *15*, 6987–6998. [CrossRef]
100. Mutahir, S.; Khurram, A.; Humayun, M.; Khan, M.A. Layered double hydroxide (LDH)/doped graphitic carbon nitride heterostructures: Design, fabrication, and applications. *Coord. Chem. Rev.* **2026**, *549*, 217360. [CrossRef]
101. Chebanenko, M.I.; Zakharova, N.V.; Lobinsky, A.A.; Popkov, V.I. Ultrasonic-Assisted Exfoliation of Graphitic Carbon Nitride and its Electrocatalytic Performance in Process of Ethanol Reforming. *Semiconductors* **2019**, *53*, 2072–2077. [CrossRef]
102. Su, J.; Zhu, L.; Geng, P.; Chen, G. Self-assembly graphitic carbon nitride quantum dots anchored on $TiO_2$ nanotube arrays: An efficient heterojunction for pollutants degradation under solar light. *J. Hazard. Mater.* **2016**, *316*, 159–168. [CrossRef] [PubMed]
103. Mitchell, E.; Law, A.; Godin, R. Experimental determination of charge carrier dynamics in carbon nitride heterojunctions. *Chem. Commun.* **2021**, *57*, 1550–1567. [CrossRef] [PubMed]
104. Pan, Z.; Wang, S.; Niu, P.; Liu, M.; Wang, X. Photocatalytic overall water splitting by spatially-separated Rh and RhOx cocatalysts on polymeric carbon nitride nanosheets. *J. Catal.* **2019**, *379*, 129–137. [CrossRef]
105. An, X.; Hu, C.; Lan, H.; Liu, H.; Qu, J. Strongly Coupled Metal Oxide/Reassembled Carbon Nitride/Co–Pi Heterostructures for Efficient Photoelectrochemical Water Splitting. *ACS Appl. Mater. Interfaces* **2018**, *10*, 6424–6432. [CrossRef] [PubMed]
106. Han, X.; Kang, Y.; Lu, R.; Yu, A. Salt promoted metallic Pt photodeposition on graphitic carbon nitride towards efficiently photocatalytic hydrogen evolution. *J. Catal.* **2024**, *436*, 115629. [CrossRef]
107. Shah, Y.; Gilbertson, L.M. Tuning Reactive Species Production of Graphitic Carbon Nitride via Oxygen Doping. *ACS Sustain. Chem. Eng.* **2025**, *13*, 18915–18923. [CrossRef]
108. Liu, Z.; Jiang, X.; Li, Z.; Zheng, Y.; Nie, J.J.; Cui, Z.; Liang, Y.; Zhu, S.; Chen, D.; Wu, S. Recent progress of photo-excited antibacterial materials via chemical vapor deposition. *Chem. Eng. J.* **2022**, *437*, 135401. [CrossRef]
109. Wang, Z.; Walker, G.W.; Muir, D.C.G.; Nagatani-Yoshida, K. Toward a global understanding of chemical pollution: A first comprehensive analysis of national and regional chemical inventories. *Environ. Sci. Technol.* **2020**, *54*, 2575–2584. [CrossRef] [PubMed]
110. Ali, H.; Orooji, Y.; Al Alwan, B.; Jery, A.E.; Alhashmialameer, D.; Abu-Dief, A.M.; Guo, S.R.; Hayat, A.; Pei, L. Unlocking the potential of MOFs-based heterojunction photocatalysts: Synthesis, modification, and performance enhancement. *Renew. Sustain. Energy Rev.* **2026**, *226*, 116359. [CrossRef]
111. Ray, J.P.; Chandrasekar, R.; Sathasivam, J.; Narayanasamy, S. Unveiling the photocatalytic potential of mesoporous carbon nitride in environmental applications: Properties, synthesis and doping strategies. *J. Environ. Chem. Eng.* **2025**, *13*, 115945. [CrossRef]
112. Yue, S.; Zhao, Z.; Yang, M.; Liu, Y.; Wang, P.; Xie, C.; Zhan, S. Reuse emerging pollutants towards the circular economy. *Chin. Chem. Lett.* **2026**, *37*, 112108. [CrossRef]
113. Roy, S.S.; Bhuvanendran, N.; Pichiah, S.; Kuila, A.; Mishra, N.S. When microplastics meet emerging pollutants: Key insights on mechanistic features for environmental remediations. *J. Mol. Liq.* **2026**, *444*, 129227. [CrossRef]
114. Nguyen, V.T.H.; Nguyen, B.T.T.; Nguyen, H.T.; Pham, N.X. Synthesizing a ternary $TiO_2$@g-$C_3N_4$/UiO-66 photocatalyst from waste polyethylene terephthalate plastic to treat polystyrene microplastics in polluted water. *ChemNanoMat* **2026**, *12*, 202500677. [CrossRef]
115. Jia, R.; Li, D.; Wang, P.; Li, T.; Chen, J.; Zhang, L.Y.; Zhao, Q.; Cheng, X. Constructing Z-scheme $MoO_{3-x}$/g-$C_3N_4$ heterojunction for highly efficient photocatalytic degradation of microplastic polyaniline. *Appl. Surf. Sci.* **2026**, *715*, 164506. [CrossRef]
116. Lu, Y.; Gao, S.; Ma, T.; Zhang, J.; Liu, H.; Zhou, W. A Z-Scheme Heterojunction g-$C_3N_4$/$WO_3$ for Efficient Photodegradation of Tetracycline Hydrochloride and Rhodamine B. *Nanomaterials* **2025**, *15*, 410. [CrossRef] [PubMed]
117. Rohan Khizer, M.; Saddique, Z.; Imran, M.; Javaid, A.; Latif, S.; Mantzavinos, D.; Momotko, M.; Boczkaj, G. Polymer and graphitic carbon nitride based nanohybrids for the photocatalytic degradation of pharmaceuticals in wastewater treatment—A review. *Sep. Purif. Technol.* **2024**, *350*, 127768. [CrossRef]
118. Guo, X.; Cheng, C.; Di, M.; Zhang, Y.; Wang, H.; Shou, R.; Lu, S.; Cao, S. Dual-functional iron thiophosphate/graphitic carbon nitride photocatalytic system for antibiotics degradation and bacterial inhibition. *Sep. Purif. Technol.* **2026**, *394*, 137537. [CrossRef]
119. Zheng, X.; Ye, J.; Luo, J.; Liu, B.; Ren, H.; Labidi, A.; Zhao, Z.; Wang, X. Efficient degradation and detoxification of tetracycline over g-$C_3N_4$/$Cr_2O_3$ S-scheme heterojunction under visible light: Mechanism insight and biotoxicity evaluation. *J. Environ. Chem. Eng.* **2025**, *13*, 117702. [CrossRef]

120. Navidpour, A.H.; Safaei, J.; Johir, M.A.H.; Ni, B.J.; Dashti, A.; Li, X.; Zhou, J.L. Zinc oxide@citric acid-modified graphitic carbon nitride nanocomposites for adsorption and photocatalytic degradation of perfluorooctanoic acid. *Adv. Compos. Hybrid Mater.* **2024**, *7*, 53. [CrossRef]
121. Kang, Y.; Leng, X.; Jin, X.; Chen, F.; Duan, H.; Cao, B. Oxygen vacancy-rich Z-scheme g-$C_3N_4$/BiOBr heterojunction with enhanced visible-light photocatalytic activity for pollutants degradation. *Mater. Sci. Eng. B* **2025**, *319*, 118341. [CrossRef]
122. Zhang, X.; Li, W.; Hu, L.; Gao, M.; Feng, J. A Tight-Connection g-$C_3N_4$/BiOBr (001) S-Scheme Heterojunction Photocatalyst for Boosting Photocatalytic Degradation of Organic Pollutants. *Nanomaterials* **2024**, *14*, 1071. [CrossRef] [PubMed]
123. Rodríguez-Hernández, J.A.; Araújo, R.G.; López-Pacheco, I.Y.; Rodas-Zuluaga, L.I.; González-González, R.B.; Parra-Arroyo, L.; Sosa-Hernández, J.E.; Melchor-Martínez, E.M.; Martínez-Ruiz, M.; Barceló, D.; et al. Environmental persistence, detection, and mitigation of endocrine disrupting contaminants in wastewater treatment plants—A review with a focus on tertiary treatment technologies. *Environ. Sci. Adv.* **2022**, *1*, 680–704. [CrossRef]
124. Duan, Y.; Li, J.; Li, Y.; Shang, X.; Jia, D.; Li, C. Direct Z-scheme $Bi_2O_2CO_3$/porous g-$C_3N_4$ heterojunction for improved photocatalytic degradation performance. *J. Taiwan Inst. Chem. Eng.* **2020**, *106*, 74–85. [CrossRef]
125. Masekela, D.; Mafa, P.J.; Yusuf, T.L.; Balogun, S.A.; Kuvarega, A.T.; Modibane, K.D. Recent advances in MXene-based nanocomposites for photocatalytic wastewater treatment, carbon dioxide reduction, and hydrogen production: A comprehensive review. *Coord. Chem. Rev.* **2026**, *549*, 217270. [CrossRef]
126. Zhao, G.; Ding, J.; Zhou, F.; Chen, X.; Wei, L.; Gao, Q.; Wang, K.; Zhao, Q. Construction of a visible-light-driven magnetic dual Z-scheme $BiVO_4$/g-$C_3N_4$/$NiFe_2O_4$ photocatalyst for effective removal of ofloxacin: Mechanisms and degradation pathway. *Chem. Eng. J.* **2021**, *405*, 126704. [CrossRef]
127. Dai, Y.; Feng, Z.; Zhong, K.; Tian, J.; Wu, G.; Liu, Q.; Wang, Z.; Hua, Y.; Liu, J.; Xu, H.; et al. Highly efficient and exceptionally durable photooxidation properties on $Co_3O_4$/g-$C_3N_4$ surfaces. *Materials* **2023**, *16*, 3879. [CrossRef] [PubMed]
128. Richardson, S.D.; Plewa, M.J.; Wagner, E.D.; Schoeny, R.; DeMarini, D.M. Occurrence, genotoxicity, and carcinogenicity of regulated and emerging disinfection by-products in drinking water: A review and roadmap for research. *Mutat. Res. Rev. Mutat. Res.* **2007**, *636*, 178–242. [CrossRef] [PubMed]
129. Zhan, S.; Hou, Q.; Li, Y.; Ma, S.; Wang, P.; Li, Y.; Wang, H. AgBr/g-$C_3N_4$ nanocomposites for enhanced visible-light-driven photocatalytic inactivation of *Escherichia coli*. *RSC Adv.* **2018**, *8*, 34428–34436. [CrossRef] [PubMed]
130. Zhang, J.; Wang, W.; Huang, S.; Lv, Y.; Li, M.; Wu, M.; Wang, H. Metal-free photocatalyst with reduced graphene oxide-doped graphitic carbon nitride homojunctions for efficient antibacterial applications. *RSC Adv.* **2025**, *15*, 2444–2451. [CrossRef] [PubMed]
131. Chen, J.; Lin, W.; Xie, L.; Huang, J.; Wang, W. Templated fabrication of graphitic carbon nitride with ordered mesoporous nanostructures for high-efficient photocatalytic bacterial inactivation under visible light irradiation. *J. Nanomater.* **2019**, *2019*, 3242136. [CrossRef]
132. Zhang, Y.; Su, S.; Zhang, Y.; Zhang, X.; Giusto, P.; Huang, X.; Liu, J. Visible-light-driven photocatalytic water disinfection toward Escherichia coli by nanowired g-$C_3N_4$ film. *Front. Nanotechnol.* **2021**, *3*, 684788. [CrossRef]
133. Ali, H.; Khan, E.; Ilahi, I. Environmental chemistry and ecotoxicology of hazardous heavy metals: Environmental persistence, toxicity, and bioaccumulation. *J. Chem.* **2019**, *2019*, 6730305. [CrossRef]
134. Chen, X.; Zhang, Y.; Yuan, D.; Huang, W.; Ding, J.; Wan, H.; Dai, W.L.; Guan, G. One step method of structure engineering porous graphitic carbon nitride for efficient visible-light photocatalytic reduction of Cr(VI). *J. Mater. Sci. Technol.* **2021**, *71*, 211–220. [CrossRef]
135. Zhang, W.; Li, L.; Gao, Y.; Zhang, D. Graphitic carbon nitride-based materials for photocatalytic reduction of U(VI). *New J. Chem.* **2020**, *44*, 19961–19976. [CrossRef]
136. Yi, X.-H.; Ma, S.-Q.; Du, X.-D.; Zhao, C.; Fu, H.; Wang, P.; Wang, C.-C. The Facile Fabrication of 2D/3D Z-Scheme g-$C_3N_4$/UiO-66 Heterojunction with Enhanced Photocatalytic Cr(VI) Reduction Performance under White Light. *Chem. Eng. J.* **2019**, *375*, 121944. [CrossRef]
137. Ding, L.; Deng, Y.; Liu, X.; Liu, L.; Ding, J.; Deng, F. Photocatalytic Reduction of Cr(VI) and Degradation of Organic Pollutants by Z-Scheme g-$C_3N_4$/$Bi_2S_3$ Heterojunction. *J. Chem. Eng. Res. Updates* **2022**, *9*, 1–12. [CrossRef]
138. Dai, Z.; Zhen, Y.; Sun, Y.; Li, L.; Ding, D. $ZnFe_2O_4$/g-$C_3N_4$ S-scheme photocatalyst with enhanced adsorption and photocatalytic activity for uranium(VI) removal. *Chem. Eng. J.* **2021**, *415*, 129002. [CrossRef]
139. Wang, L.; Song, H.; Yuan, L.; Li, Z.; Zhang, Y.; Gibson, J.K.; Zheng, L.; Chai, Z.; Shi, W. Efficient U(VI) reduction and sequestration by $Ti_3C_2T_x$ MXene. *Environ. Sci. Technol.* **2018**, *52*, 10748–10756. [CrossRef] [PubMed]
140. Dai, Z.R.; Liang, B.C.; Chen, L.J.; Zhang, W.L.; Gao, Y.; Li, L. Rational construction of S-scheme $ZnIn_2S_4$/g-$C_3N_4$ heterojunction for effective sacrificial agent-free uranium photocatalysis in air. *Sep. Purif. Technol.* **2025**, *354*, 129241. [CrossRef]
141. Liu, Y.; Wu, S.; Liu, J.; Xie, S.; Liu, Y. Synthesis of g-$C_3N_4$/$TiO_2$ nanostructures for enhanced photocatalytic reduction of U(VI) in water. *RSC Adv.* **2021**, *11*, 4810–4817. [CrossRef] [PubMed]

142. Liu, Z.; Li, Y.; Yao, S.; Zhou, R.; Lin, G.; Fu, Y.; Zhou, Q.; Wang, W.; Chi, W. Rich electron delocalization structure in carbon nitride inducing radical transfer for high-performance photocatalytic uranyl reduction. *Carbon Energy* **2024**, *6*, 636. [CrossRef]
143. Ajiboye, T.O.; Oyewo, O.A.; Marzouki, R.; Onwudiwe, D.C. Photocatalytic reduction of hexavalent chromium using $Cu_{3.21}Bi_{4.79}S_9$/g-$C_3N_4$ nanocomposite. *Catalysts* **2022**, *12*, 1075. [CrossRef]
144. Yang, K.; Yang, Y.; Jiang, Y.; Ye, B.; Li, L.; Liu, W.; Yan, T.; Li, W.; Liu, S. Controlled synthesis of $Bi_2S_3$/g-$C_3N_4$ nanosheets for efficient degradation of Rhodamine B and reduction of Cr(VI) under visible light. *Surf. Interfaces* **2024**, *52*, 104885. [CrossRef]
145. Song, X.Y.; Chen, Q.L. Facile preparation of g-$C_3N_4$/$Bi_2WO_6$ hybrid photocatalyst with enhanced visible light photoreduction of Cr(VI). *J. Nanopart. Res.* **2019**, *21*, 183. [CrossRef]
146. Hasija, V.; Raizada, P.; Singh, P.; Verma, N.; Khan, A.A.P.; Singh, A.; Selvasembian, R.; Kim, S.Y.; Hussain, C.M.; Nguyen, V.H.; et al. Progress on the photocatalytic reduction of hexavalent Cr(VI) using engineered graphitic carbon nitride. *Process Saf. Environ. Prot.* **2021**, *152*, 663–678. [CrossRef]

**Disclaimer/Publisher's Note:** The statements, opinions and data contained in all publications are solely those of the individual author(s) and contributor(s) and not of MDPI and/or the editor(s). MDPI and/or the editor(s) disclaim responsibility for any injury to people or property resulting from any ideas, methods, instructions or products referred to in the content.